
Congested C(*sp*³)-rich architectures enabled by iron-catalysed conjunctive alkylation

In the format provided by the authors and unedited

Density Functional Theory (DFT) Calculations

Computational methods

Kohn-Sham density functional theory (KS-DFT) calculations were performed with *Gaussian 16* rev. B.01³². Geometry optimizations were performed using the B3LYP hybrid functional³³⁻³⁶ with Grimme's D3 dispersion correction with Becke-Johnson damping³⁷ (hereafter denoted B3LYP-D3BJ) and the def2-SVP³⁸ Karlsruhe-family basis set for all atoms. Minima and transition structures on the potential energy surface (PES) were confirmed using harmonic frequency analysis at the same level of theory, showing respectively zero and one imaginary frequency. Where needed, intrinsic reaction coordinate (IRC)^{39,40} analysis were carried out to connect the appropriate reactant/product states passing through a given transition state. Single point (SP) corrections were performed using B3LYP-D3BJ and def2-TZVP⁷ basis set for all atoms. The SMD implicit continuum solvation model⁴¹ was used to account for the effect of tetrahydrofuran (THF) solvent on the computed Gibbs energy profile. Gibbs energies were evaluated at the reaction temperature of 60 °C, using Grimme's scheme of quasi-RRHO treatment of vibrational entropies⁴², using the GoodVibes code⁴³. Vibrational entropies of frequencies below 100 cm⁻¹ were obtained according to a free rotor description, using a smooth damping function to interpolate between the two limiting descriptions. The free energies reported in Gaussian from gas-phase optimisation were further corrected using standard concentration of 1 mol/L,⁴⁴⁻⁴⁶ which were used in solvation calculations, instead of the gas-phase 1atm used by default in Gaussian program.

To further assess that our level of theory is appropriate, we performed separately single-point energy calculations for all chemical species in our study using the global-hybrid meta-NGA (nonseparable gradient approximation) MN15 functional⁴⁷ with def2-TZVP basis set in implicit solvation of THF using SMD solvation model. This functional was chosen as it performs much better than many other functionals in predicting transition metal reaction barrier heights⁴⁷ and has the ability to model multi-reference systems that may be involved in iron catalysed radical systems. MN15 has been shown to give better agreement in reproducing the energetic profile of trinuclear Cu-catalysed methane-to-methanol catalytic conversion⁴⁸ than many other functionals including ω B97X-D and TPSS.

Unless otherwise stated, the final SMD (THF)-B3LYP-D3BJ/def2-TZVP//B3LYP-D3BJ/def2-SVP and SMD (THF)-MN15/def2-TZVP//B3LYP-D3BJ/def2-SVP Gibbs

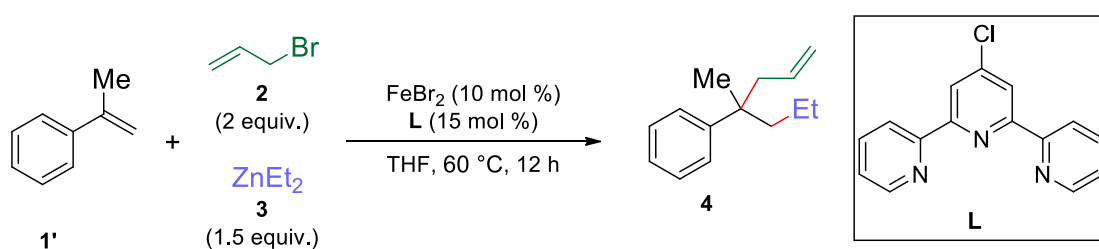
energies are given with the latter set of values given in brackets; the former set of values are used for discussion throughout. For example, if the relative values for a species is given as 14.7 (15.1) kcal/mol, then the value of 14.7 kcal/mol is obtained from SMD (THF)-B3LYP-D3BJ/def2-TZVP//B3LYP-D3BJ/def2-SVP whereas the value of 15.1 kcal/mol is obtained from SMD (THF)-MN15/def2-TZVP//B3LYP-D3BJ/def2-SVP. *All Gibbs energy values in the text and figures are quoted in kcal/mol.*

For species involving open-shell characteristics, including doublet, triplet, quartet, quintet and sextet radicals, we performed above-mentioned DFT methodologies using the unrestricted formalism of the Kohn-Sham theory (UKS-DFT). The eigenvalues of the spin operator S^2 after annihilation of spin contamination were checked to ensure that they comply with the expected value of $S(S+1) = 0.75$ for a doublet wavefunction and $S(S+1) = 2$ for triplet, $S(S+1) = 3.75$ for quartet, $S(S+1) = 6$ for quintet, $S(S+1) = 8.75$ for sextet, indicating that spin contamination is not a problem for the present methodology.

All molecular structures and spin density plots were visualized using *PyMOL*⁴⁹ and *GaussView*⁵⁰ software.

Model reaction

Supplementary Figure 19 shows the model reaction that we used for computational studies of reaction mechanism for the present Fe-catalyzed conjunctive alkylation of alkenes.



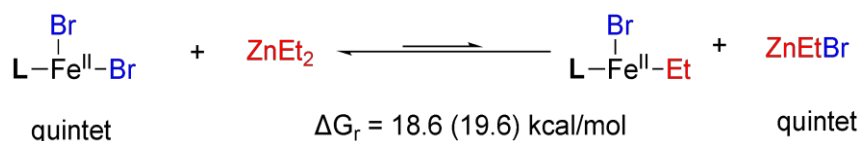
Supplementary Figure 19. Model reaction used in computational modelling.

Iron(II) pathway

7.3.1 Thermodynamics for the generation of active catalytic species

The thermodynamics for the generation of Fe(II) species **Fe(II)[L]EtBr (I)** from **Fe(II)[L]Br₂** was determined computationally. Species **Fe(II)[L]Br₂** is the most stable in the quintet state, with the triplet state that is 14.0 (10.9) kcal/mol higher and the singlet state 21.5 (30.3) kcal/mol higher. The Fe(II) species **Fe(II)[L]EtBr (I)** is most stable in the quintet spin state (**I_{quintet}**) and is lower in energy by 9.7 (10.5) kcal/mol

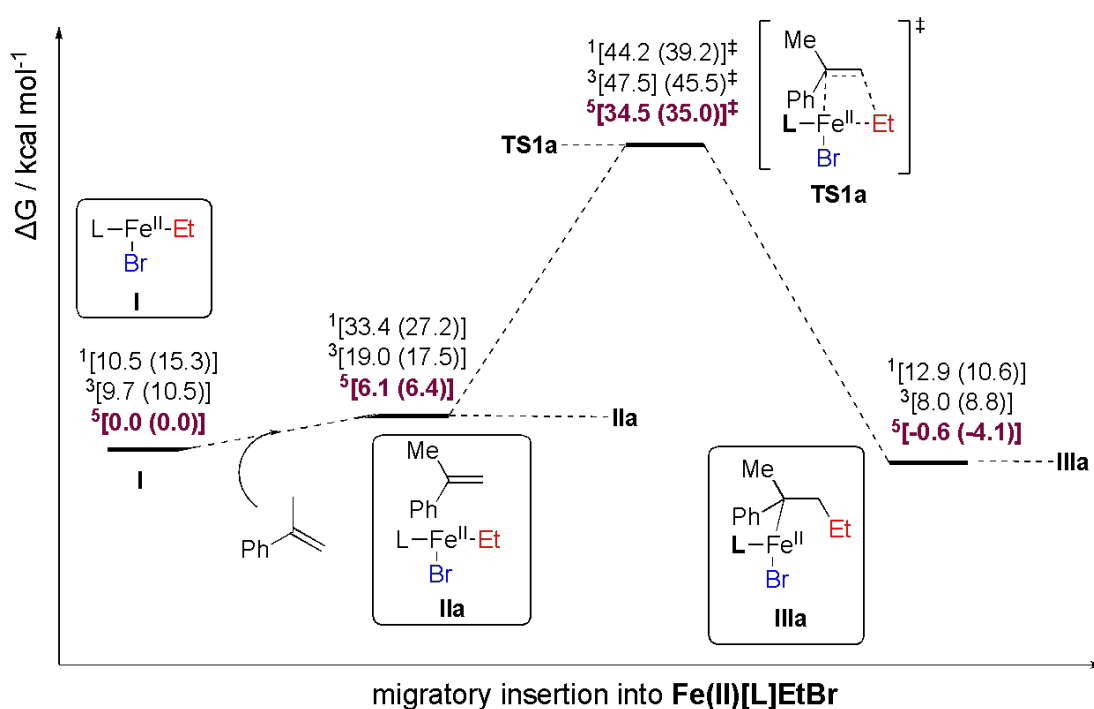
compared to its triplet spin state (**I_triplet**) and by 10.5 (15.3) kcal/mol compared to its singlet spin state (**I_singlet**). The Gibbs energy for the following transformation



was determined to be 18.6 (19.6) kcal/mol. Although thermodynamically uphill, this process is thermally accessible at the reaction temperature of 60 °C, allowing the generation of the active catalytic species **Fe(II)[L]EtBr (I)**.

7.3.2 Migratory Insertion step

7.3.2.1 Concerted mechanism



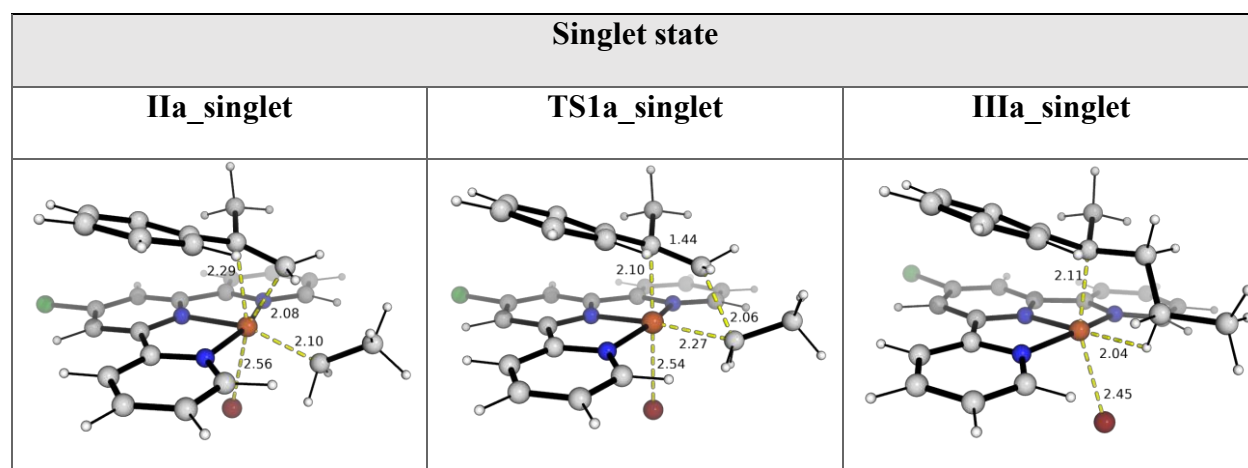
Supplementary Figure 20. Gibbs energy profile for the migratory insertion step of styrene substrate into Fe(II) species in different spin states. The superscript on the left indicates the spin states, 1 = singlet; 3 = triplet; 5 = quintet. Values in square brackets are obtained at SMD (THF)-B3LYP-D3BJ/def2-TZVP//B3LYP-D3BJ/def2-SVP level of theory and values in round brackets are obtained at SMD (THF)-MN15/def2-TZVP//B3LYP-D3BJ/def2-SVP level of theory. **L** = ligand as shown in Supplementary Figure 19.

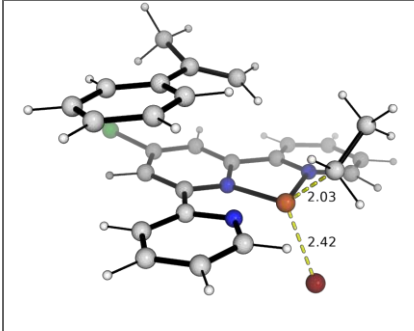
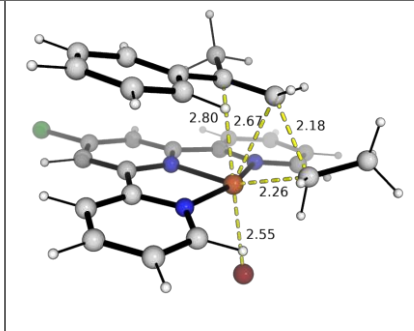
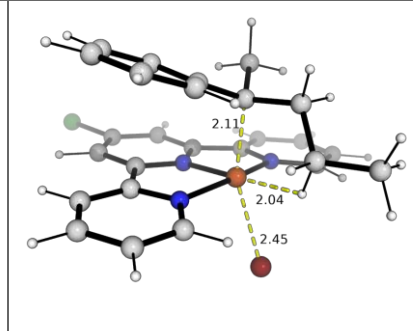
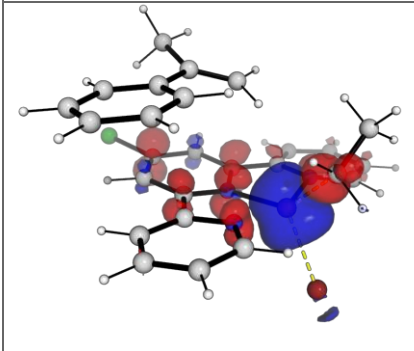
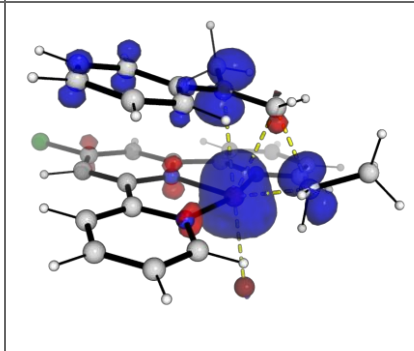
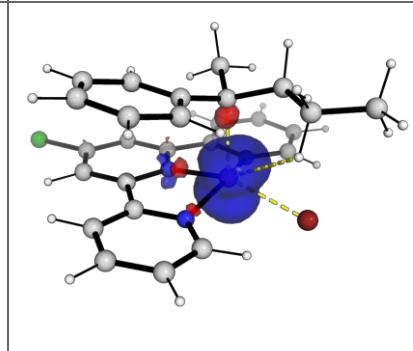
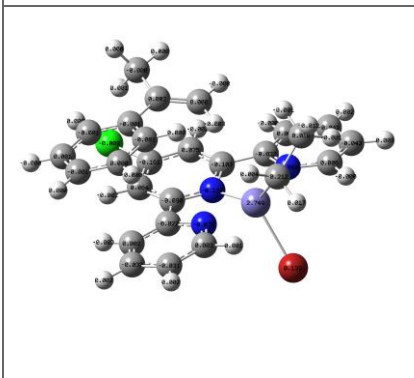
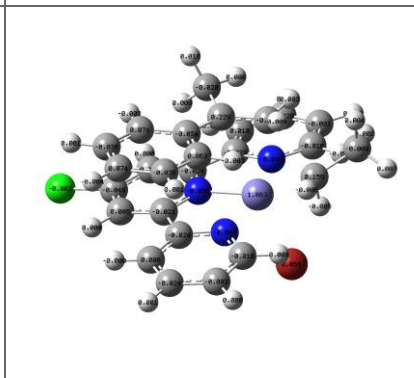
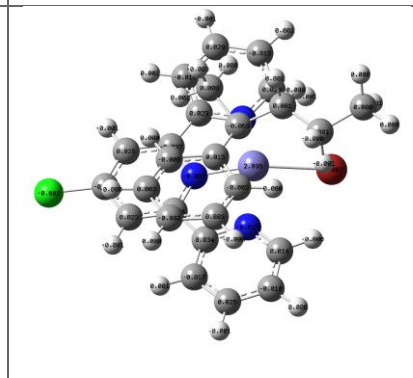
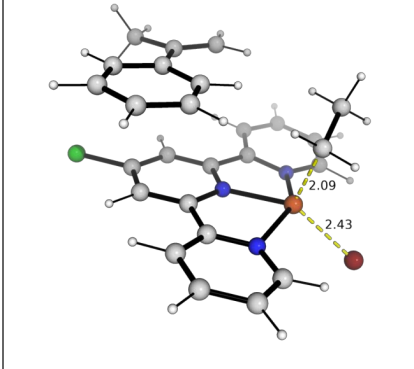
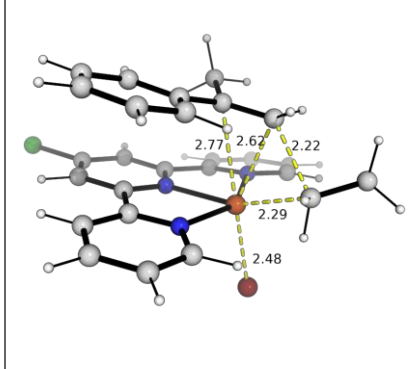
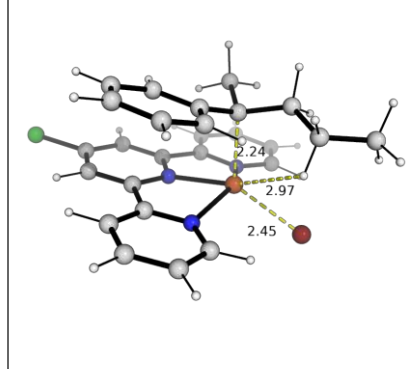
The Gibbs energy profile for the concerted migratory insertion of styrene substrate into Fe(II)-C(Et) bond is shown in Supplementary Figure 20. The concerted migratory

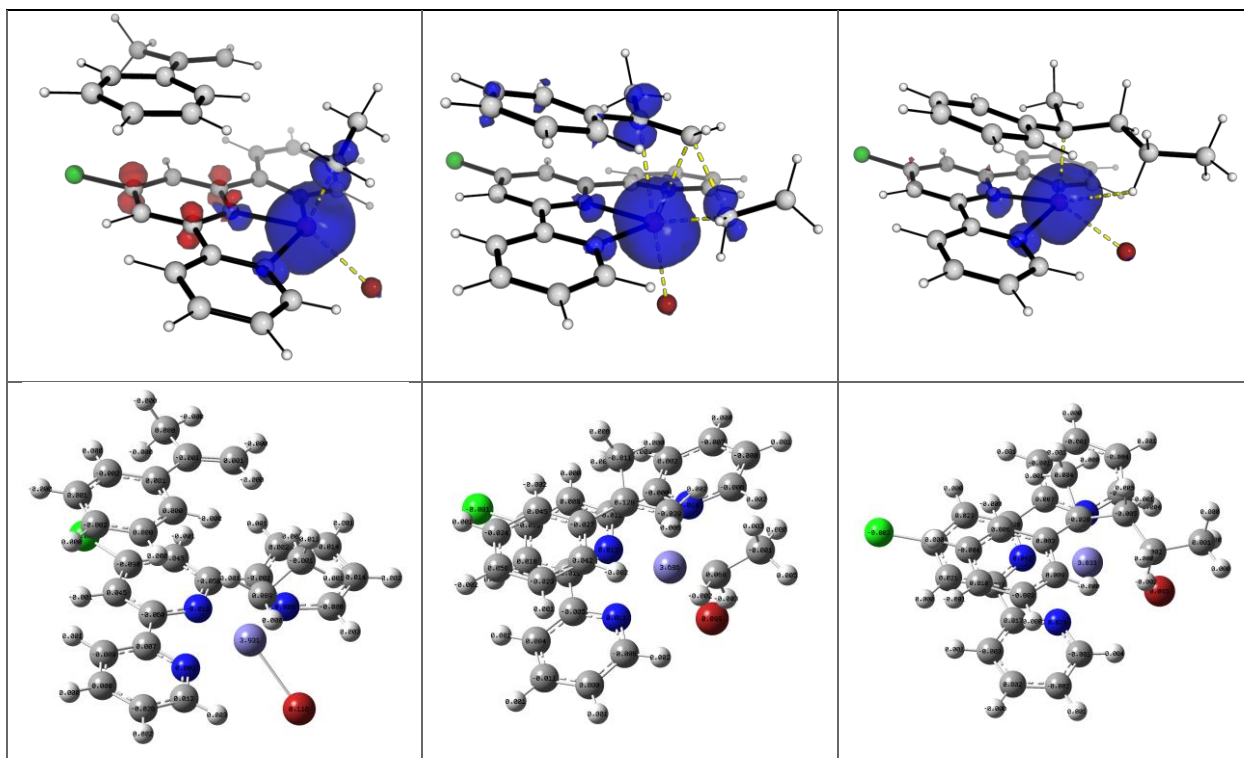
insertion of styrene in the quintet spin state, **TS1a_quintet**, has a barrier of 34.5 (35.0) kcal/mol whereas in the triplet and singlet spin states, this barrier is 47.5 (45.5) kcal/mol and 44.2 (39.2) kcal/mol, respectively. The concerted migratory insertion of styrene into the Fe(II)–C(Et) bond thus likely occur in the high-spin quintet state with a barrier of 34.5 (35.0) kcal/mol.

The DFT-optimised structures for the migratory insertions in Fe(II) in different spin states and their spin density plots (for open-shell systems, triplet and quintet states) are shown in Supplementary Figure 21. Visualization of these TSs show that the migratory insertion step occurs via a concerted mechanism at all spin states [see movies (uploaded to <https://zenodo.org/record/8174459>) of the IRC runs connecting the reactant through the TS to the product for the lowest barrier spin quintet state].

For both triplet and quintet spin states, we observe that in the reactant complex, there is no radical/spin density localised on the styrene substrate, consistent with its neutral, closed shell characteristics. In the TSs, we observe the localisation of some spin density on the tertiary sp^3 carbon of the styrene substrate, indicating the formation of radical on the substrate as the insertion takes place. The spin density plots as well as the Mulliken spin population on each atom is shown in Supplementary Figure 21 for the triplet and quintet spin states. These results are consistent with our conclusion that styrene substrate is in neutral, singlet state before insertion and forms some radical characteristics in the TS as insertion takes place. The associated .log files for the Mulliken spin population analyses have been uploaded to <https://zenodo.org/record/8174459>, for ease of visualisation by the readers.



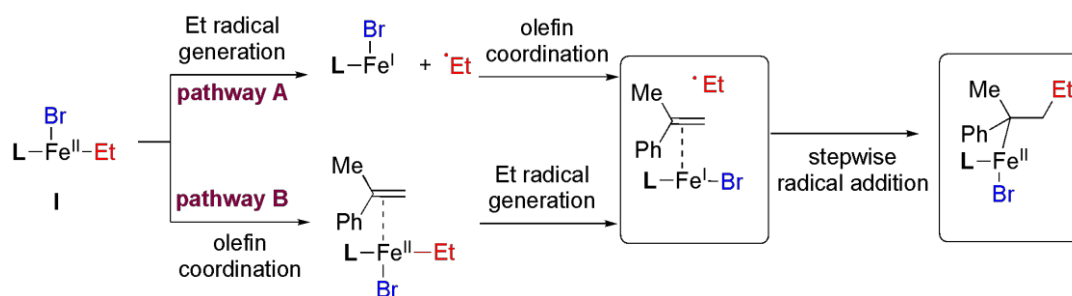
Triplet state		
IIa_triplet	TS1a_triplet	IIIa_triplet
		
		
		
Quintet state		
IIa_quintet	TS1a_quintet	IIIa_quintet
		



Supplementary Figure 21. DFT-optimized structures for the lowest barrier insertions in Fe(II) species and their spin density plots (for open-shell systems, triplet and quintet states, at an isovalue of 0.02 a.u.).

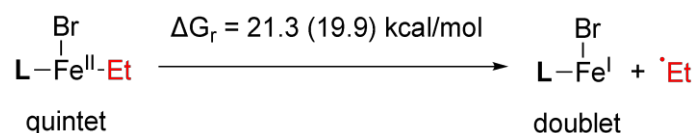
7.3.2.2 Stepwise mechanism

We explored the alternative stepwise mechanism in which the Et radical forms initially from the homolytic cleavage of Fe–C(Et) bond in the Fe(II) species **Fe(II)[L]EtBr (I)**, followed by its subsequent addition to the olefin substrate. We focus on the quintet state as complex **I** is the most stable in the quintet state. Two possible pathways were studied computationally, as shown in Supplementary Figure 22. In pathway A, the catalytic complex **I** undergoes Fe(II)–C(Et) bond cleavage to generate the Et radical, which then adds to olefin substrate that is coordinated to the resultant Fe(I) species. In pathway B, olefin substrate coordinates the catalytic complex **I**, followed by the generation of Et radical which then adds to the olefin substrate.



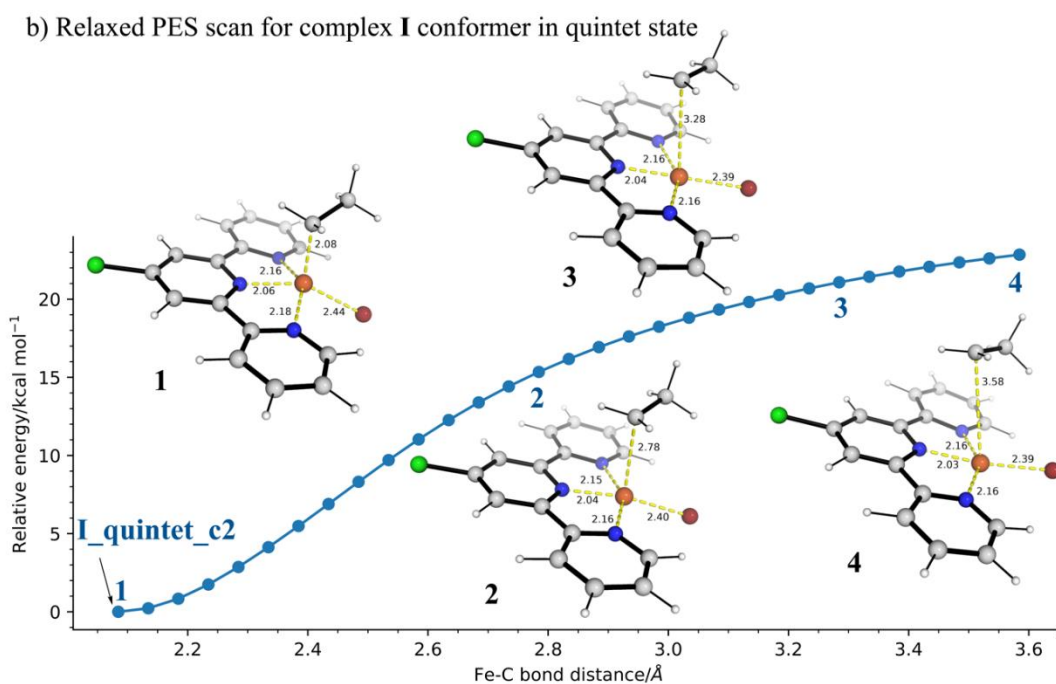
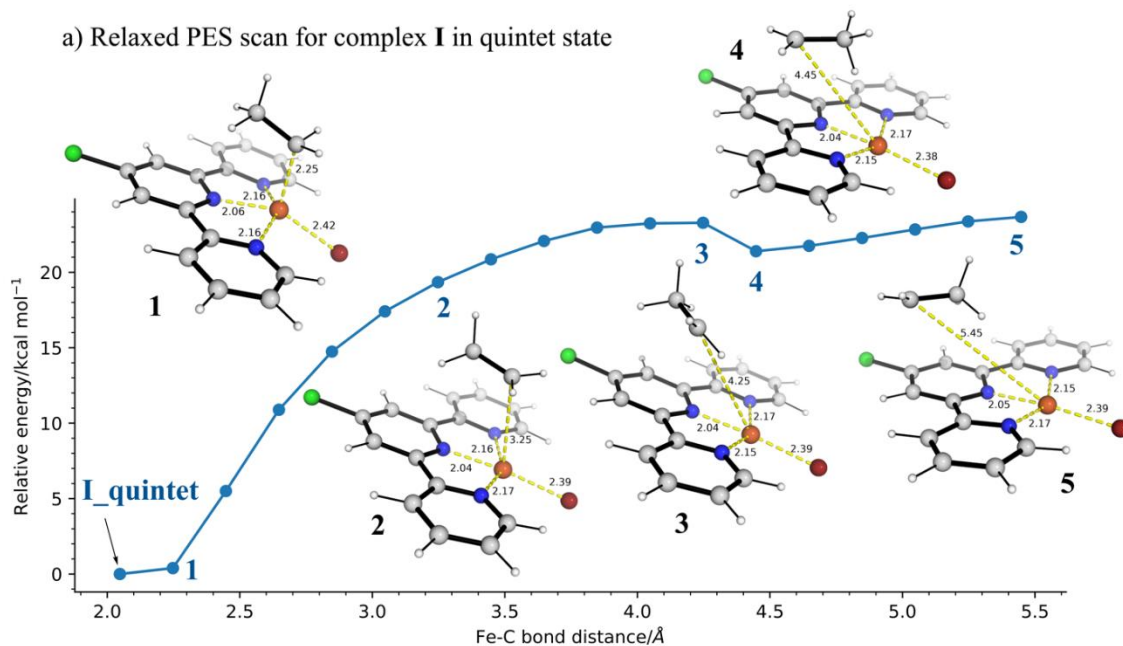
Supplementary Figure 22. Possible pathways for the stepwise generation of Et radical followed by its addition to olefin substrate.

Pathway A: The Gibbs energy of reaction for the cleavage of Fe(II)–C(Et) bond in complex **I** in pathway A was computed and we found that this is an uphill process by 21.3 (19.9) kcal/mol:

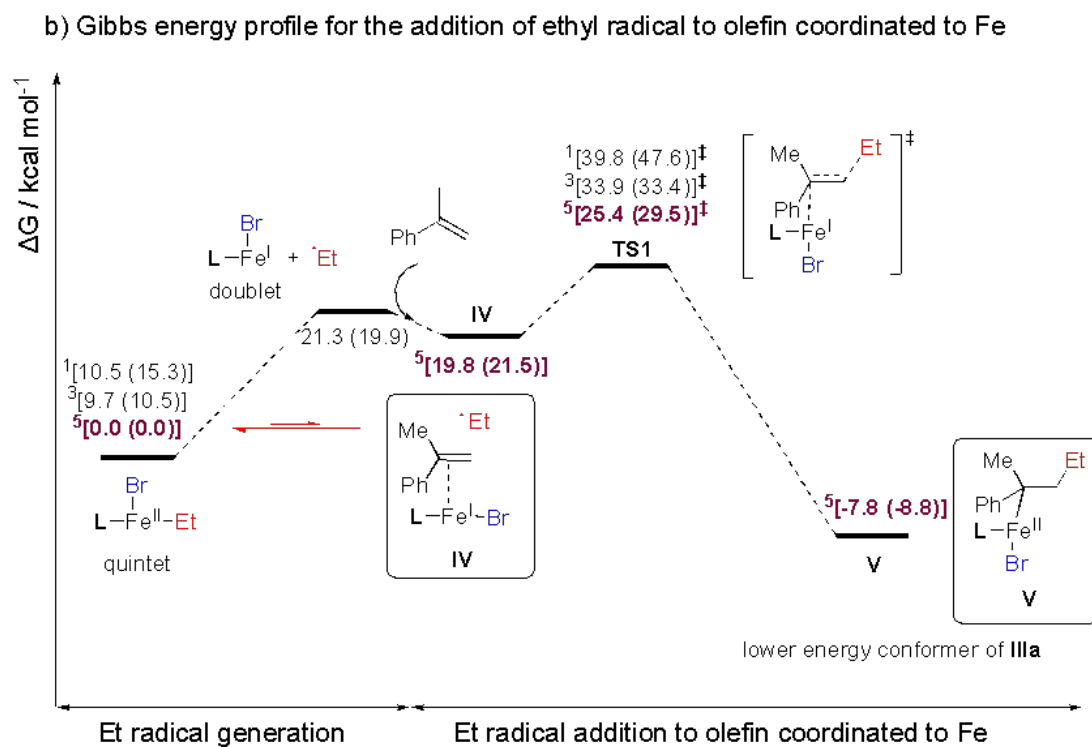
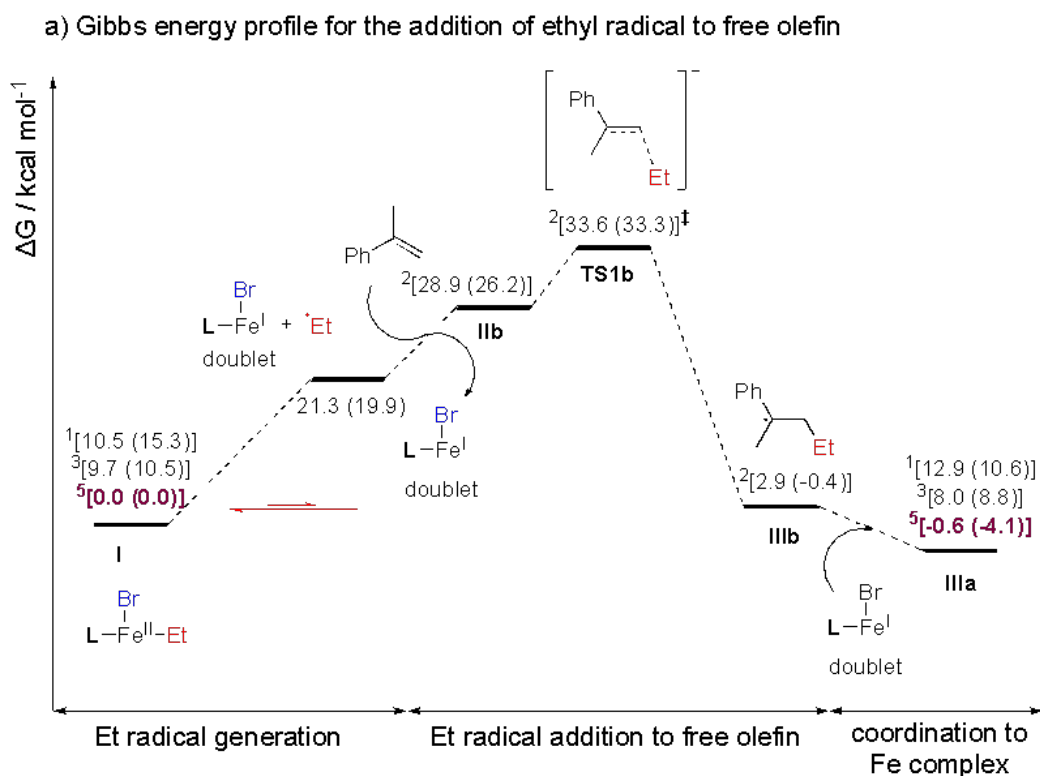


We attempted to isolate the transition state for this process, however, to no avail. A relaxed potential energy surface (PES) scan indicates that there may not be a barrier for the bond breaking of Fe–C(Et) bond and that the sum of the infinitely separated species is the highest in energy (Supplementary Figure 23). This suggests that the generation of Et radical from the homolytic cleavage of Fe(II)–C(Et) bond has a barrier that is about 21.3 (19.9) kcal/mol (required to overcome the thermodynamics) under the reaction conditions.

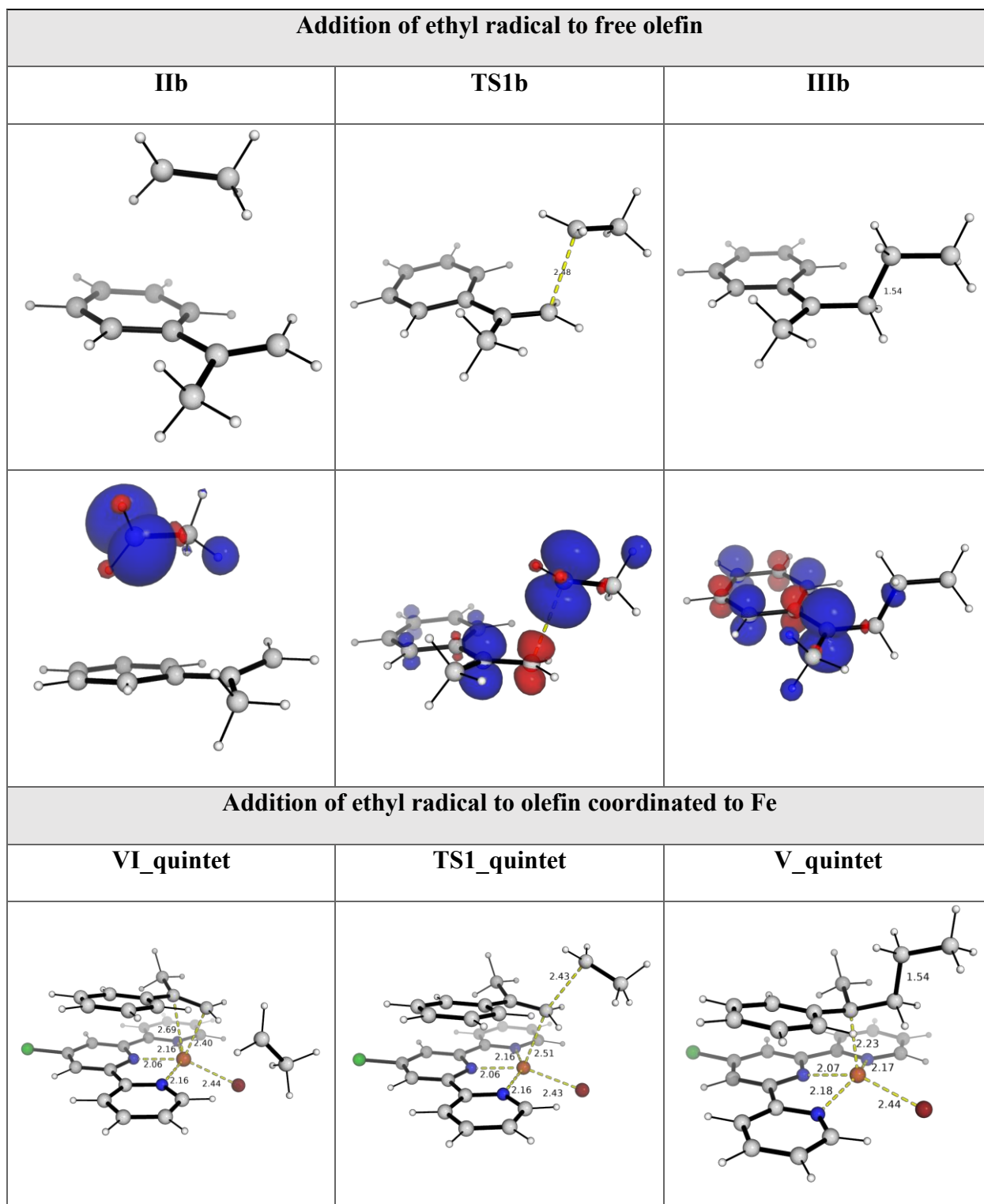
The addition of Et radical to the olefin substrate in the presence and the absence of Fe species were considered and the Gibbs energy profiles are shown in Supplementary Figure 24. The relevant DFT optimised structures and their spin density plots are shown in Supplementary Figure 25. From Supplementary Figure 24a), we can see that after homolytic cleavage of Fe–C(Et) bond to form the Et radical, the addition of Et radical to olefin after losing the Fe(I) complex has a barrier of 33.6 (33.3) kcal/mol (**TS1b**) whereas the addition of Et radical to olefin that is coordinated to the resultant Fe(I) complex has a much lower barrier of 25.4 (29.4) kcal/mol in the quintet state via **TS1**, to give thermodynamically favorable **V** at -7.8 (-8.8) kcal/mol (note that **V** and **IIIa** are conformers of the same species).

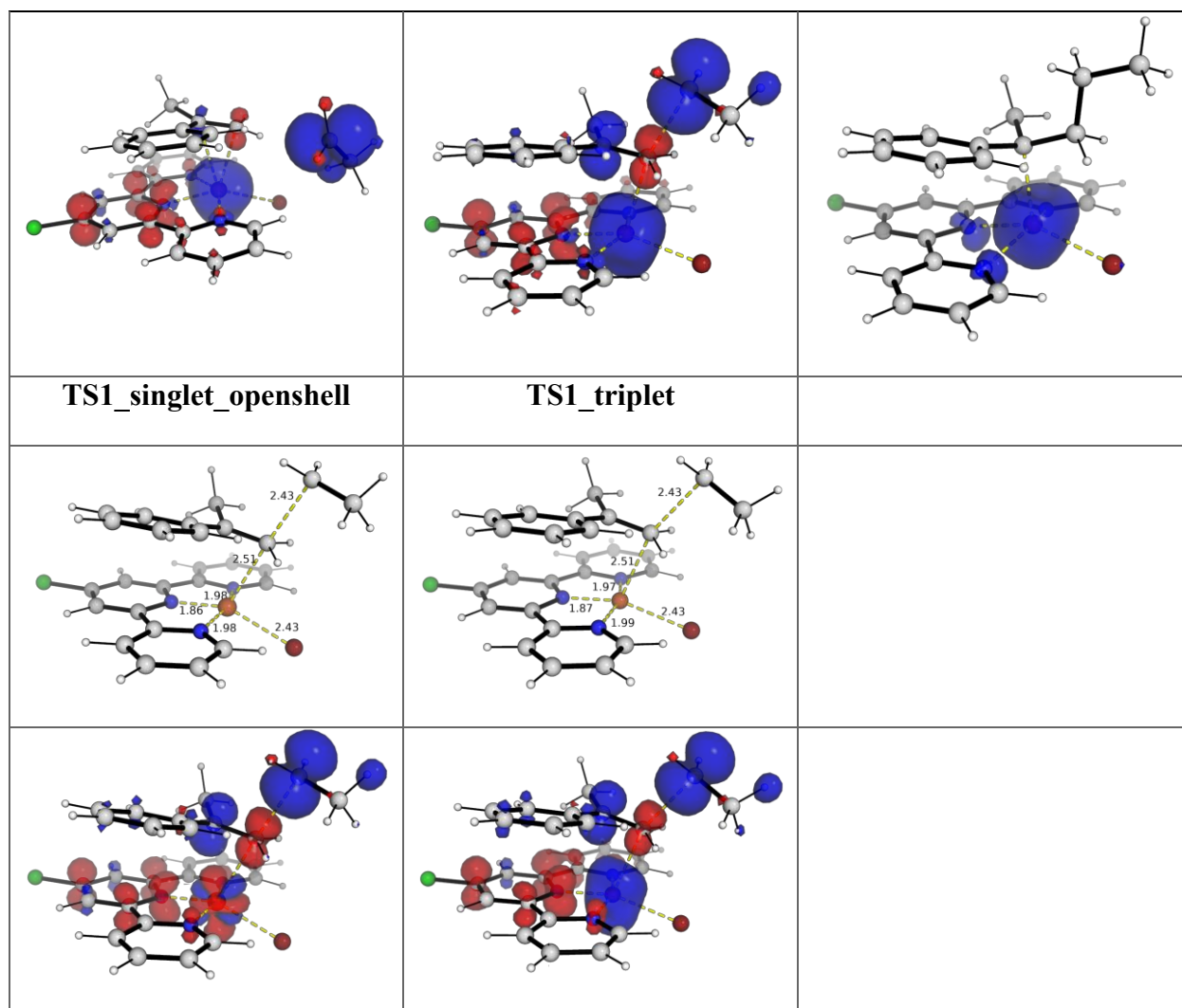


Supplementary Figure 23. Relaxed PES scan (in gas-phase using B3LYP-D3BJ/def2-SVP) energy profile along the Fe(II)–C(Et) bond in complex I in quintet state for its two conformers. B3LYP-D3BJ/def2-SVP gas-phase energy values are used without further corrections.



Supplementary Figure 24. Gibbs energy profile for the addition of ethyl radical to a) free olefin and b) olefin coordinated to Fe. The superscript on the left indicates the spin states, 1 = singlet; 3 = triplet; 5 = quintet. L = ligand as shown in Supplementary Figure 19. TS1 singlet at 39.8 (47.6) kcal/mol is openshell singlet.

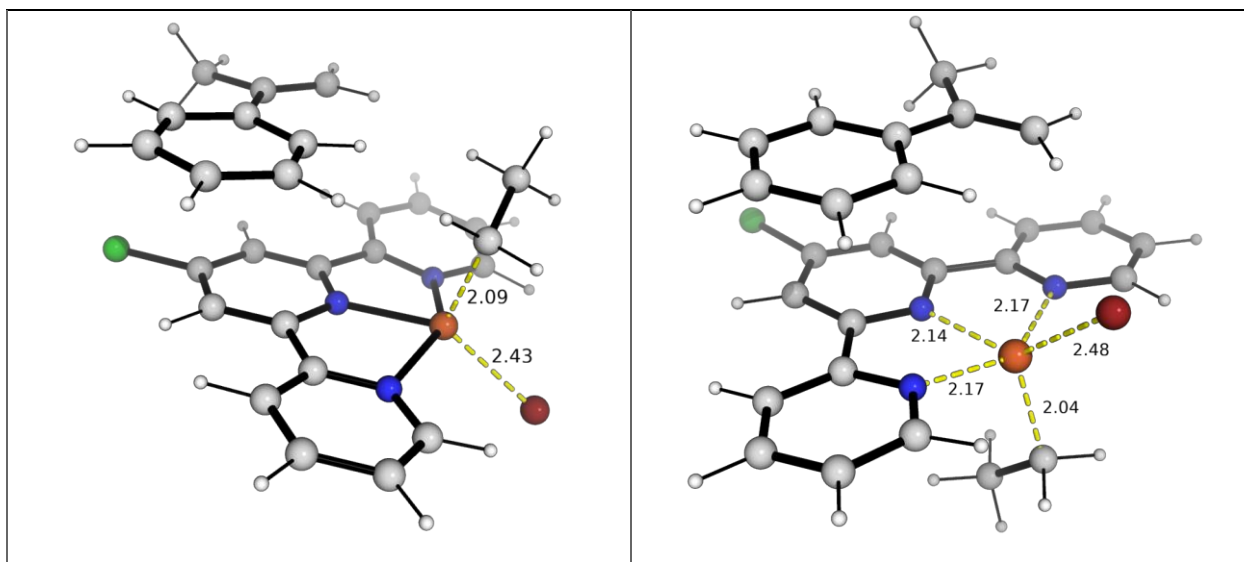




Supplementary Figure 25. DFT-optimized structures for the addition of ethyl radical to olefin substrate in the presence and absence of Fe species and their spin density plots (at an isovalue of 0.02 a.u.).

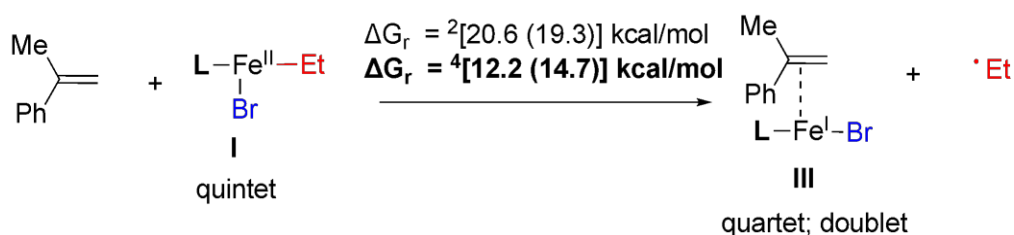
Pathway B: We explored the pathway in which the styrene substrate coordinates to Fe-centre before the generation of ethyl radical, which subsequently adds to the styrene that is coordinated to Fe-centre (Supplementary Figure 22). The styrene substrate may coordinate to either side of the Fe center, giving two different geometric isomers. The DFT optimized structures of these are shown in Supplementary Figure 26. Note that although using the styrene coordinating to Fe-center as the *initial guess structure*, these final optimised structures suggest that the C=C double bond may not be able to coordinate to the catalytic species complex **I** in quintet spin state.

IIa	II
6.1 (6.4) kcal/mol	0.9 (1.9) kcal/mol

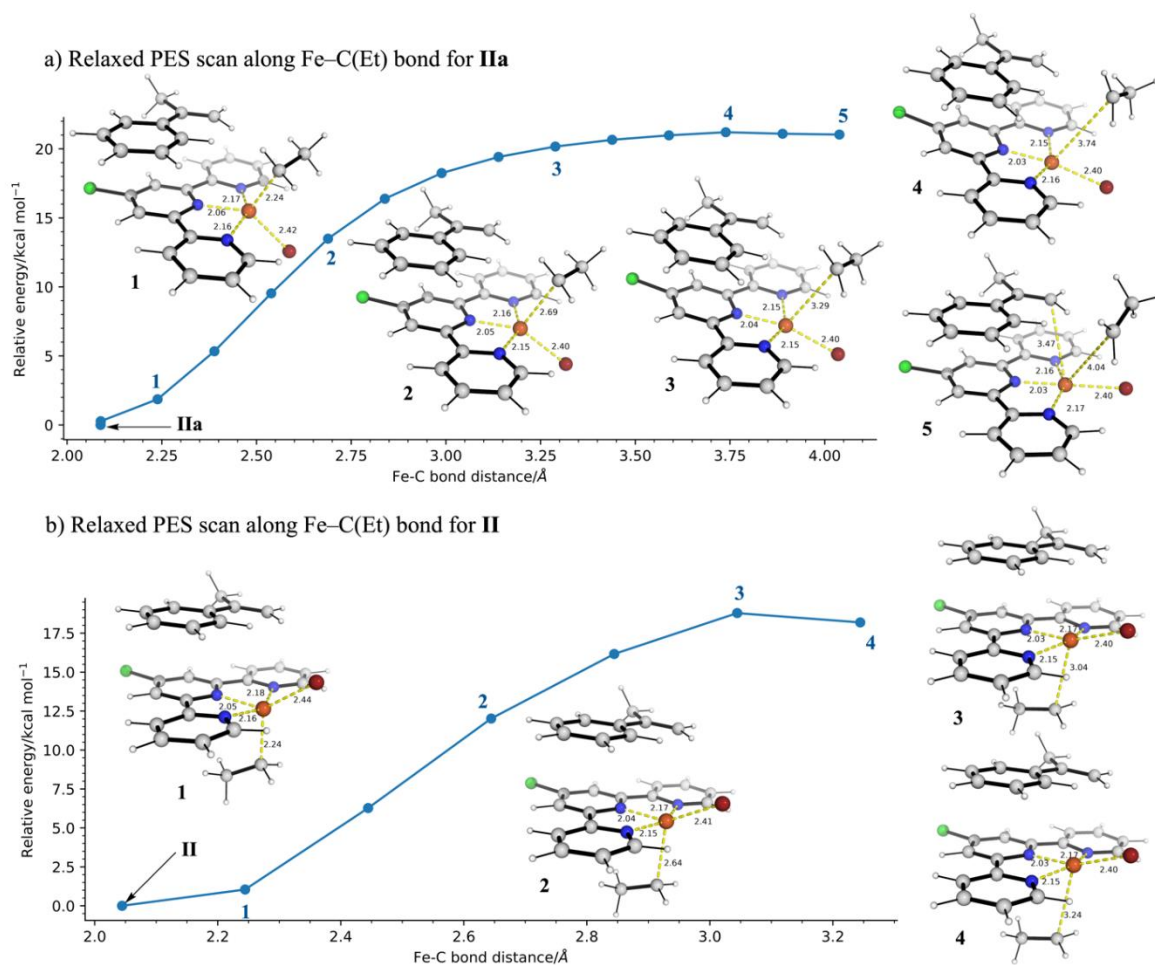


Supplementary Figure 26. DFT-optimized structures for the styrene-Fe complexes. Gibbs energies are taken relative to complex **I** in the most stable spin state, i.e., quintet.

The Gibbs energy of reaction for the generation of ethyl radical and **III** in quartet spin state is 12.2 (14.7) kcal/mol whereas that for **III** in doublet spin state is 20.6 (19.3) kcal/mol as shown below:

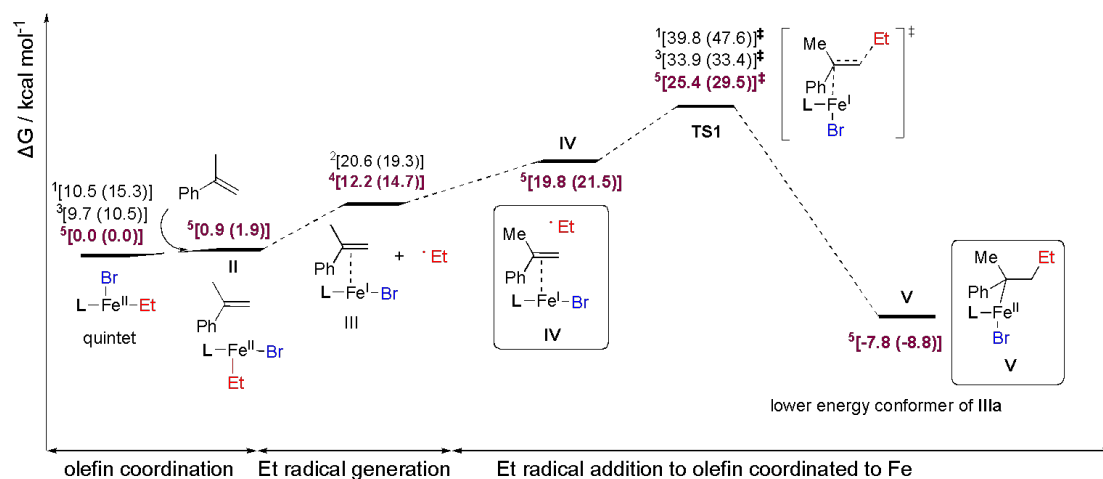


We attempted to locate the transition state structures for this process but was unsuccessful. Relaxed PES scans along the Fe(II)-C(Et) bond in **IIa** and **II** (Supplementary Figure 27) suggest that such barriers are much lower, i.e., non-rate-limiting, compared to other steps. The generation of ethyl radical from **IIa** will have a barrier of about 20 kcal/mol relative to **IIa**, therefore, this is about 26 kcal/mol above catalytic species **I** in quintet state as **IIa** is 6.1 (6.4) kcal/mol uphill of **I**. Similarly, the generation of ethyl radical from species **II** will have a barrier of about 18 kcal/mol above **I** (**II** is 0.9 (1.9) kcal/mol uphill of **I**). Thus, ethyl radical generation from **II** is more likely after styrene substrate complexes with catalytic species **I**. The energy profile for the generation of ethyl radical following styrene substrate coordination and the subsequent ethyl radical addition to Fe-coordinated styrene is shown in Supplementary Figure 28.



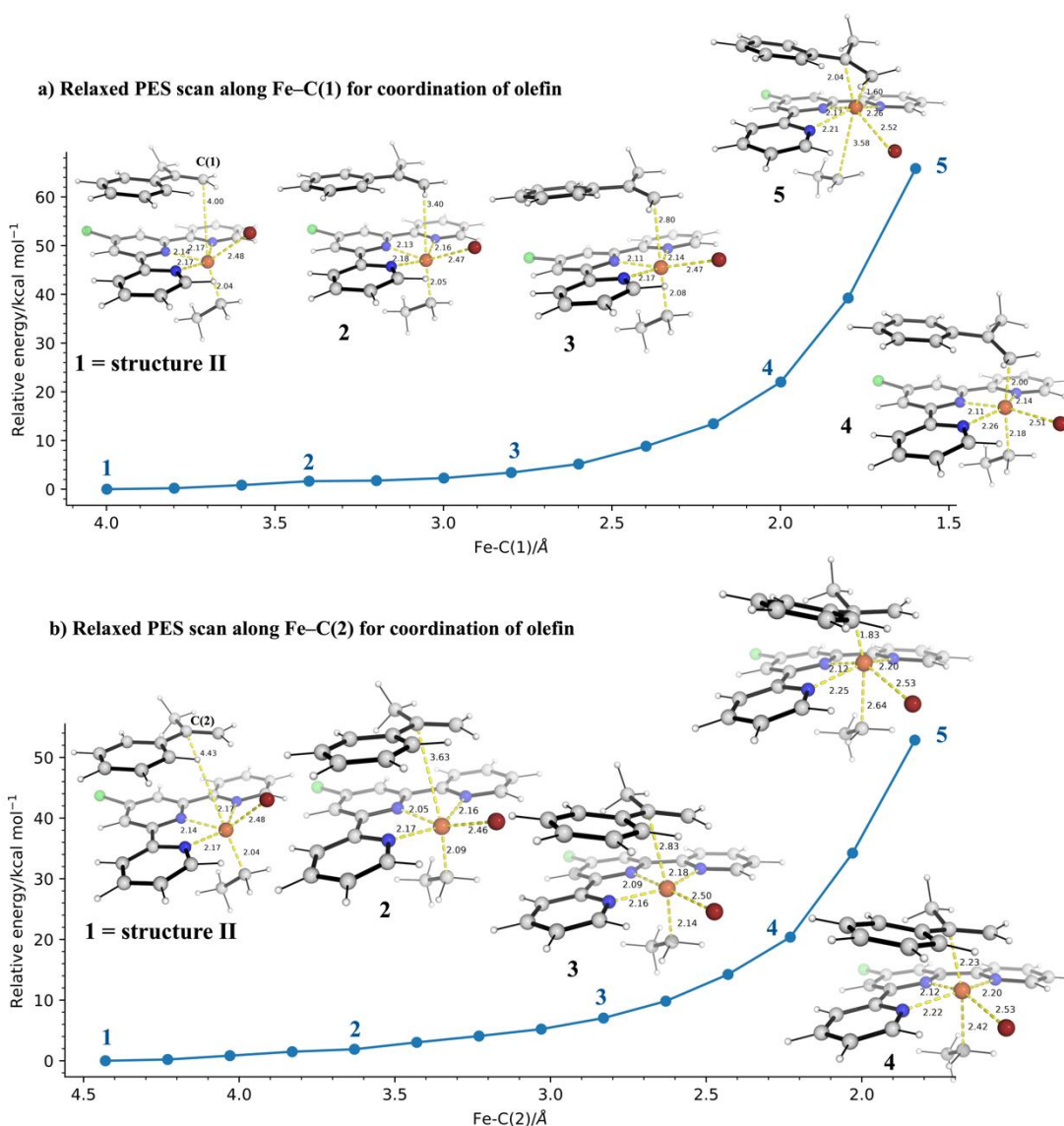
Supplementary Figure 27. Relaxed PES scan (in gas-phase using B3LYP-D3BJ/def2-SVP) energy profile along the Fe(II)–C(Et) bond in complex **IIa and **II** in quintet state. Gas-phase energy values are used without further corrections.**

Comparing the energy profiles in Supplementary Figure 24 and Supplementary Figure 28, we can see that the generation of ethyl radical occurs more readily in the presence of styrene substrate. This is potentially due to the stabilisation effect of olefin when it coordinates to the resultant LFe(I)Br species formed from LFe(II)EtBr after it undergoes Fe(II)–Et homolysis to generate the Et radical. Interestingly, species LFe(I)Br is most stable in doublet spin state, but becomes most stable in quartet spin state when it has olefin coordinated to it (complex **III**).



Supplementary Figure 28. Gibbs energy profile for the addition of ethyl radical to styrene substrate after its coordination to Fe. The superscript on the left indicates the spin states, 1 = singlet; 2 = doublet; 3 = triplet; 4 = quartet; 5 = quintet. L = ligand as shown in Supplementary Figure 19.

The relaxed PES scan were also performed by decreasing the distance of Fe–C(olefin) bond to see how the energies and structure of the Fe(II) species change as olefin approaches the Fe centre (Supplementary Figure 29). From the figure, we see that the energies increase as the Fe–C bond distance shortens. Thereby the spontaneous coordination of olefin to Fe centre is unlikely to be favoured.



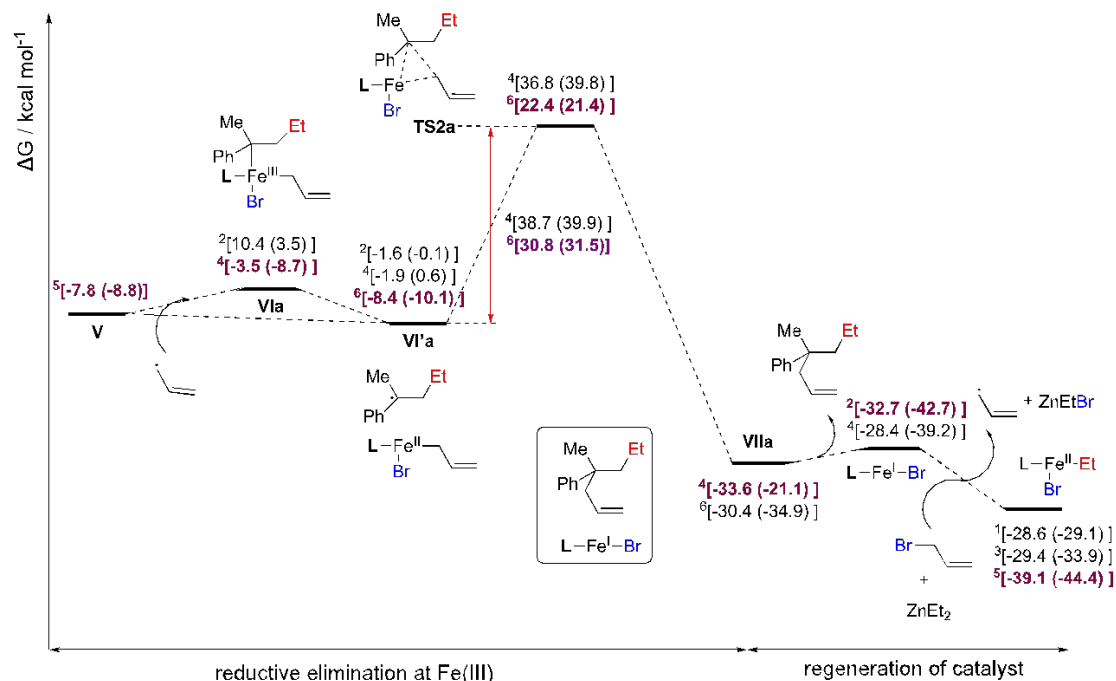
Supplementary Figure 29. Relaxed PES scan (in gas-phase using B3LYP-D3BJ/def2-SVP) energy profile along the Fe(II)–C(olefin) bond in complex II in quintet state. Gas-phase energy values are used without further corrections.

7.3.3 C–C coupling via Reductive elimination step / Inner-sphere mechanism

Once the insertion product **V**, is formed, an allyl radical can combine with it to form Fe(III) species **VIa** (Supplementary Figure 30). The addition of allyl radical to **V** to form **VIa** has a barrier that is lower than the migratory insertion and the reductive elimination step (see section 7.3.4).

Complex **VIa** upon geometry optimisation gives covalent Fe(III)–C(R) bond distance of 2.20 Å in the doublet state and 2.22 Å in the quartet state. However, direct geometry optimisation of **VIa** in the sextet state yields complex **VI'a** with an elongated Fe(III)–

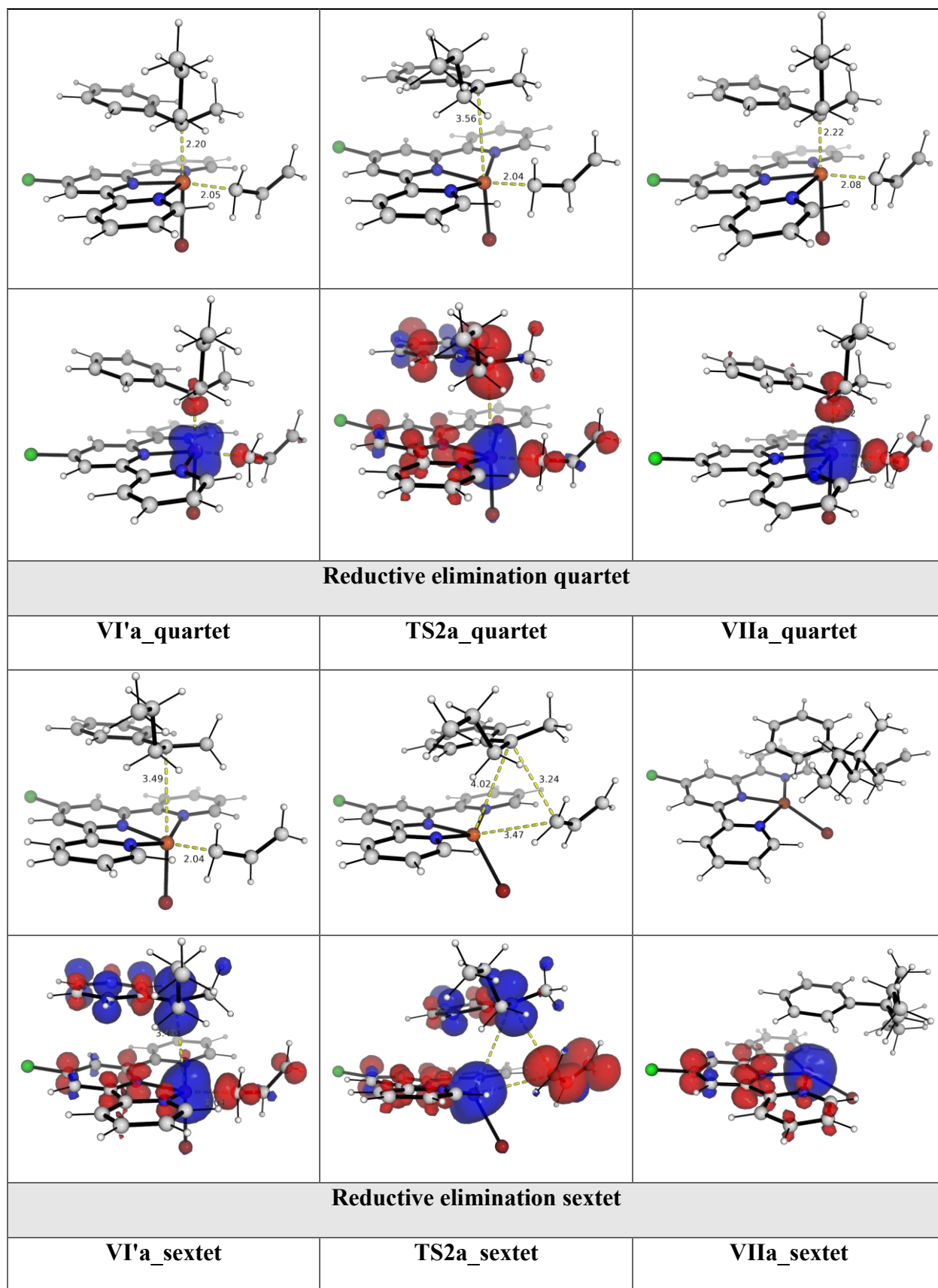
C(R) bond distance of 3.84 Å. The DFT optimised structures/energy minima for complexes **VIa** and **VI'a** are shown in Supplementary Figure 31. For both doublet and quartet spin states, complexes **VIa** and **VI'a** are in equilibrium with low barriers for their interconversion (see section 7.3.5).

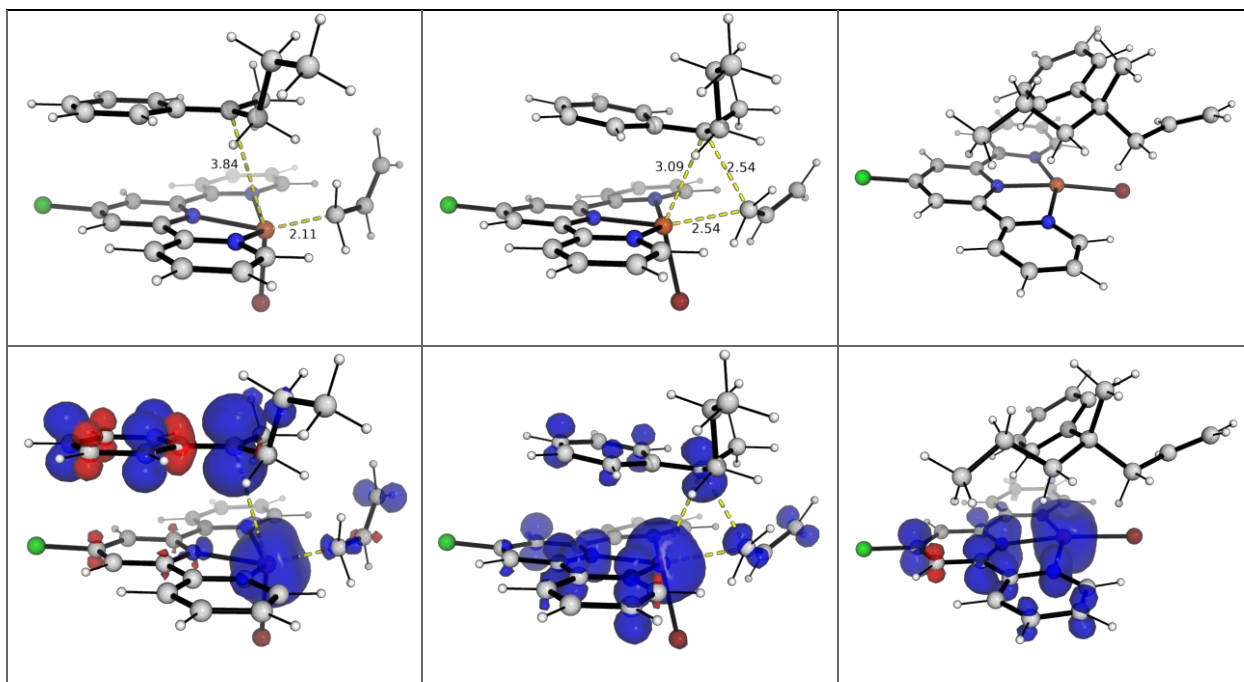


Supplementary Figure 30. Gibbs energy profile for the reductive elimination and the catalyst regeneration steps in different spin states. The superscript on the left indicates the spin states, 1 = singlet; 2 = doublet; 3 = triplet; 4 = quartet; 5 = quintet; 6 = sextet. **L** = ligand as shown in Supplementary Figure 19.

The subsequent reductive elimination from either complex **VIa** or **VI'a** in the doublet spin state is not kinetically feasible (see section 7.3.6), while the transition states for the reductive elimination from complex **VI'a** in the quartet and the sextet state have been successfully located. Supplementary Figure 31 shows the DFT optimised structures and their associated spin density plots for the reductive elimination step.

DFT-optimised structures		
VIa_doublet	VI'a_doublet	VIa_quartet

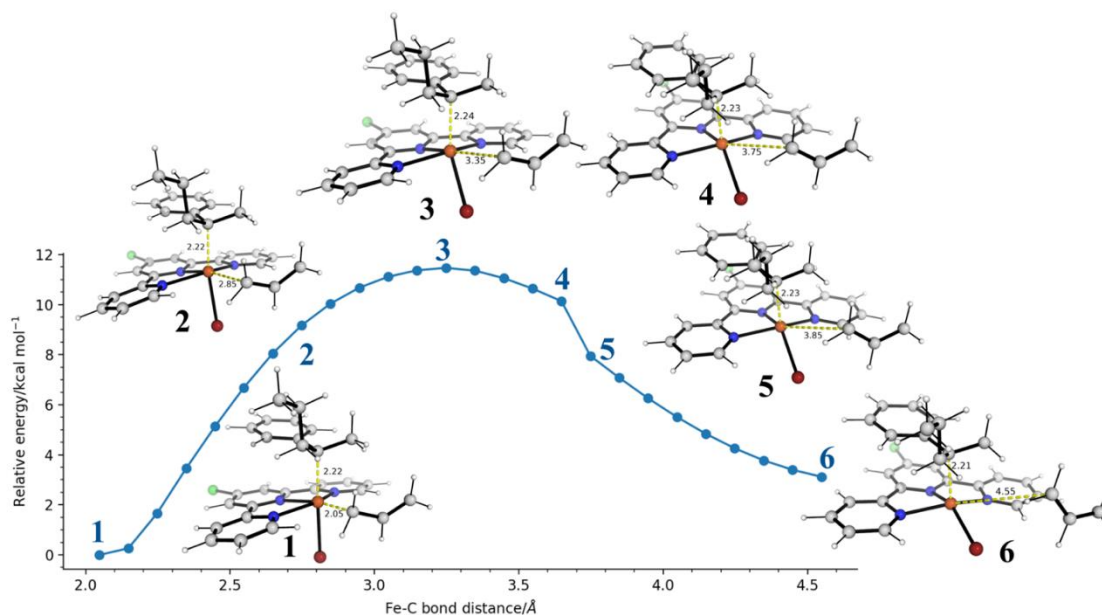




Supplementary Figure 31. DFT-optimized structures for the lowest barrier insertions in Fe(II) species and their spin density plots (for open-shell systems, triplet and quintet states, at an isovalue of 0.02 a.u.).

7.3.4 Addition of allyl radical to migratory insertion product V

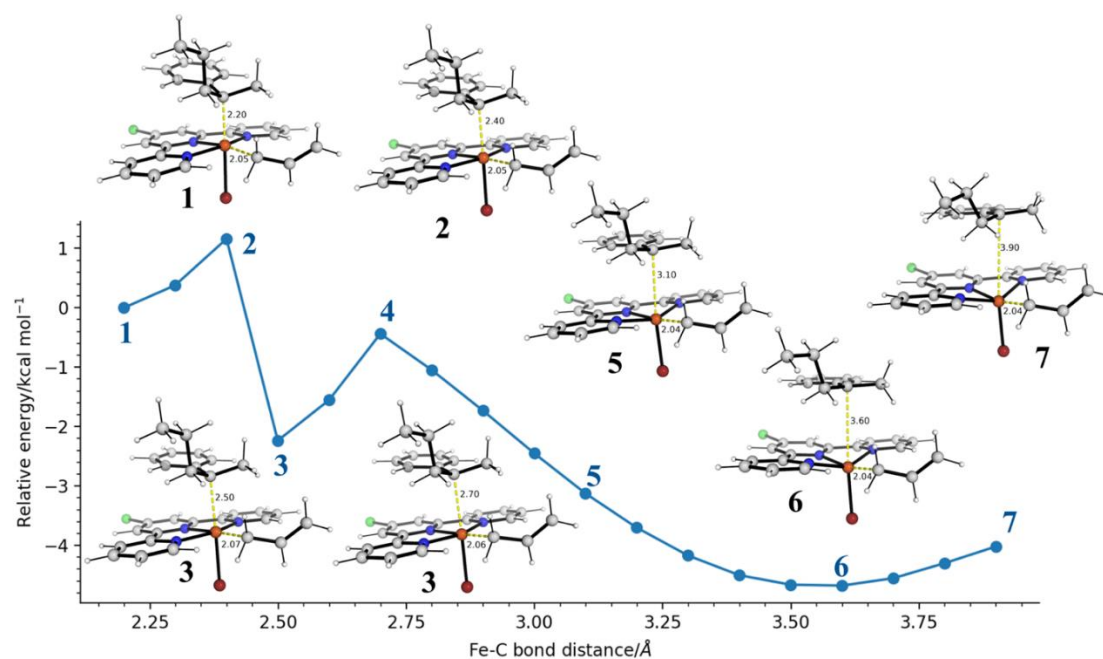
We performed a relaxed PES scan along the Fe(III)–C(allyl) bond in VI in the quartet state to find out the barrier for the addition of allyl radical to V. The relaxed PES scan energy profile shown in Supplementary Figure 32 suggests that the addition of allyl radical to V has a barrier of about <10 kcal/mol (from the right hand side to the left hand side), indicating that this will not be the critical step in the present reaction.



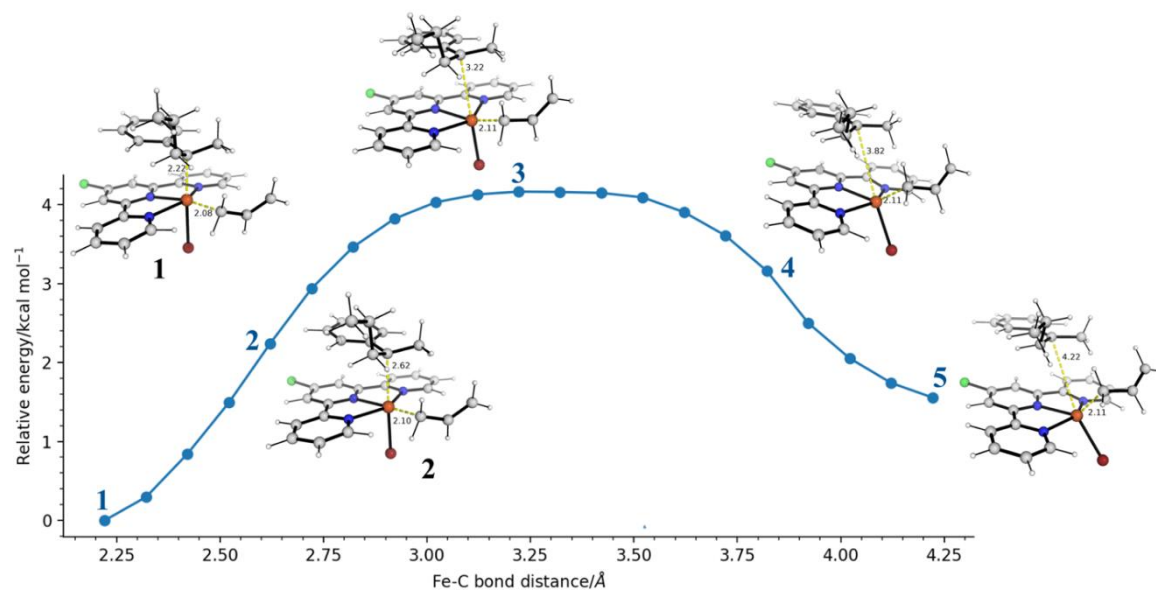
Supplementary Figure 32. Relaxed PES scan (in gas-phase using B3LYP-D3BJ/def2-SVP) energy profile along the Fe(III)–C(allyl) bond in VI in quartet state.

7.3.5 Estimation of the barrier for the conversion of VI to VI' in doublet and quartet spin states

To estimate the barrier for the conversion of VI to complex VI' in both the doublet and quartet spin state, we performed a relaxed PES scan along the Fe(III)–C(alkyl) bond in VI in both the doublet and quartet state. The relaxed PES scan energy profile shown in Supplementary Figures 33 and 34 suggests that the conversion of structure from VI with covalent Fe–C bond to VI' with elongated Fe–C bond is facile (< 5 kcal/mol in both doublet and quartet spin state), suggesting that complex VI in sextet spin state is meta-stable and that complexes VI and VI' likely exist as an equilibrium mixture.



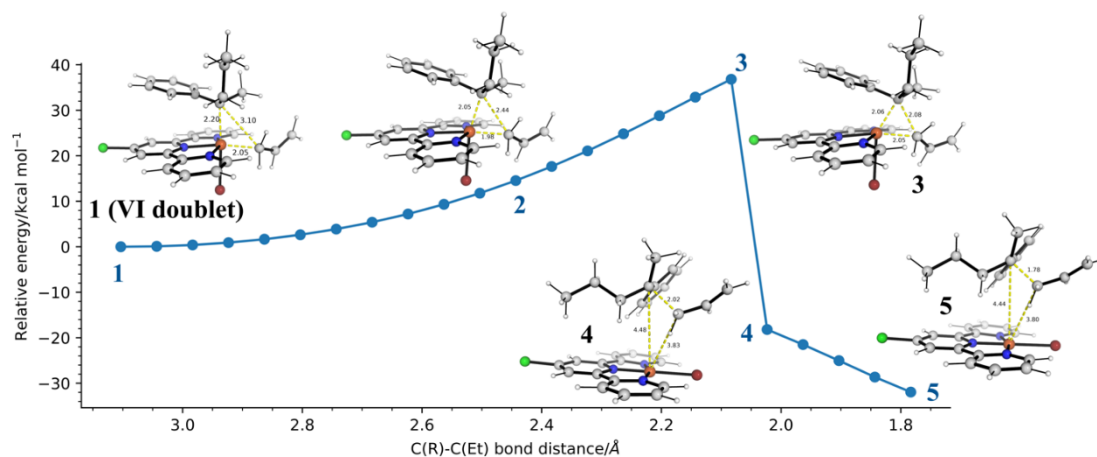
Supplementary Figure 32. Relaxed PES scan (in gas-phase using B3LYP-D3BJ/def2-SVP) energy profile along the Fe(III)–C(alkyl) bond in VI in doublet state.



Supplementary Figure 33. Relaxed PES scan (in gas-phase using B3LYP-D3BJ/def2-SVP) energy profile along the Fe(III)–C(alkyl) bond in VI in quartet state.

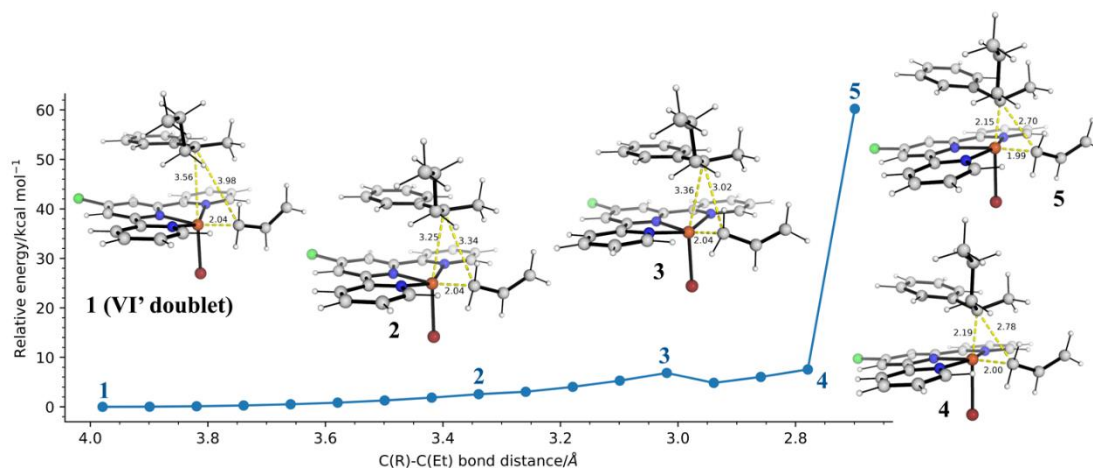
7.3.6 Estimation of the barrier for the reductive elimination from VI or VI' in doublet spin states

For completeness, herein we demonstrate that the barrier for the reductive elimination step from either VI or VI' in the doublet spin state is unfeasible kinetically under the present experimental conditions. The relaxed PES scan along the C(alkyl)–C(Et) bond distance in VI in doublet spin state as shown in Supplementary Figure 34 suggests that the reductive elimination from the Fe(III) inner coordination sphere is kinetically unfeasible as the energy keeps increasing as the C(alkyl)–C(Et) bond distance decreases. A barrier of at least 35 kcal/mol above VI in doublet state is expected before the coupling groups break away from the Fe(III) inner sphere. This is much less kinetically favorable compared to reductive elimination in the sextet state (Supplementary Figure 30). Additionally, using structure 3 in Supplementary Figure 34 as the starting guess structure did not allow us to locate the TS for the reductive elimination from VI in the doublet spin state.



Supplementary Figure 34. Relaxed PES scan (in gas-phase using B3LYP-D3BJ/def2-SVP) energy profile along the C(alkyl)–C(Et) bond in VI in doublet state.

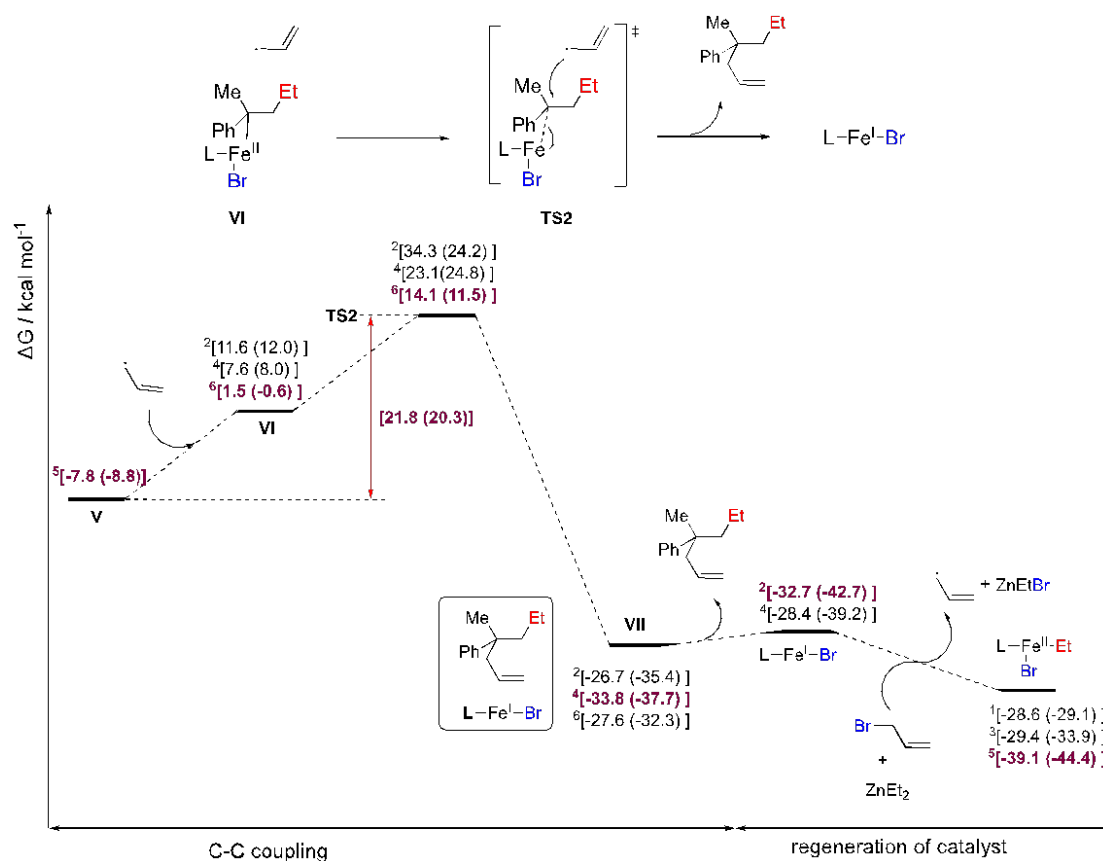
A similar PES scan along the C(alkyl)–C(Et) bond distance in VI' in doublet spin state (Supplementary Figure 35) also suggests that the reductive elimination in the doublet spin state will be highly kinetically disfavored compared to other spin states. Note structure 5 in Supplementary Figure 35, with a C(alkyl)–C(Et) bond distance of 2.70 Å, will be some structure on Supplementary Figure 34 where C(R)–C(Et) distance is 2.70 Å.



Supplementary Figure 35. Relaxed PES scan (in gas-phase using B3LYP-D3BJ/def2-SVP) energy profile along the C(alkyl)–C(Et) bond in VI' in doublet state.

7.3.7 C–C coupling via outer-sphere mechanism / radical pathway

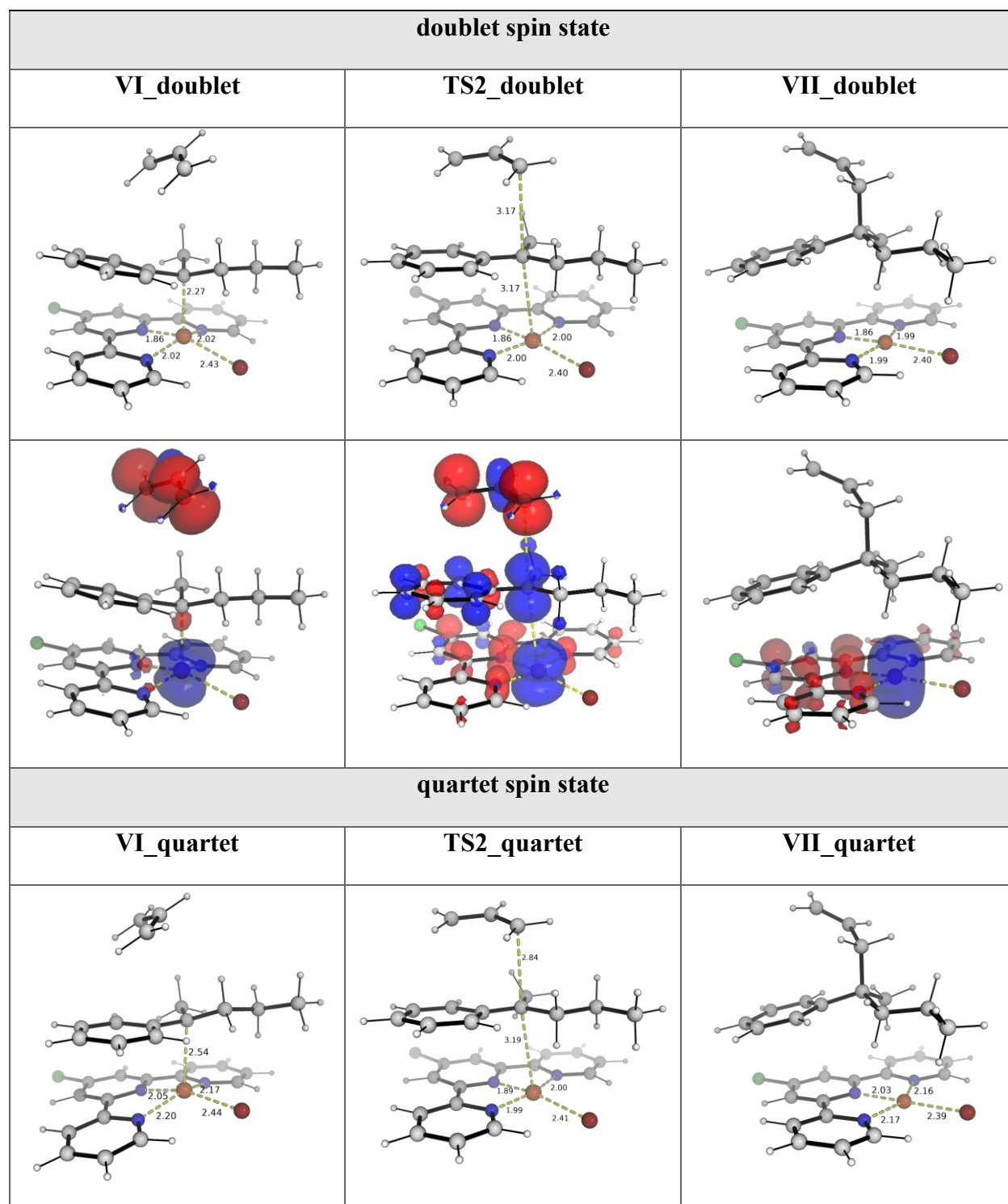
An outer-sphere mechanism for the C–C coupling step was considered and the Gibbs energy profile is shown in Supplementary Figure 36. Comparing to the inner-sphere mechanism shown in Supplementary Figure 30, where the lowest barrier for the C–C coupling step (via **TS2a** in the sextet spin state) is 30.8 (31.5) kcal/mol, the C–C coupling step via an outer-sphere mechanism (via **TS2**) has a much lower barrier of 21.8 (20.3) kcal/mol in the sextet state.

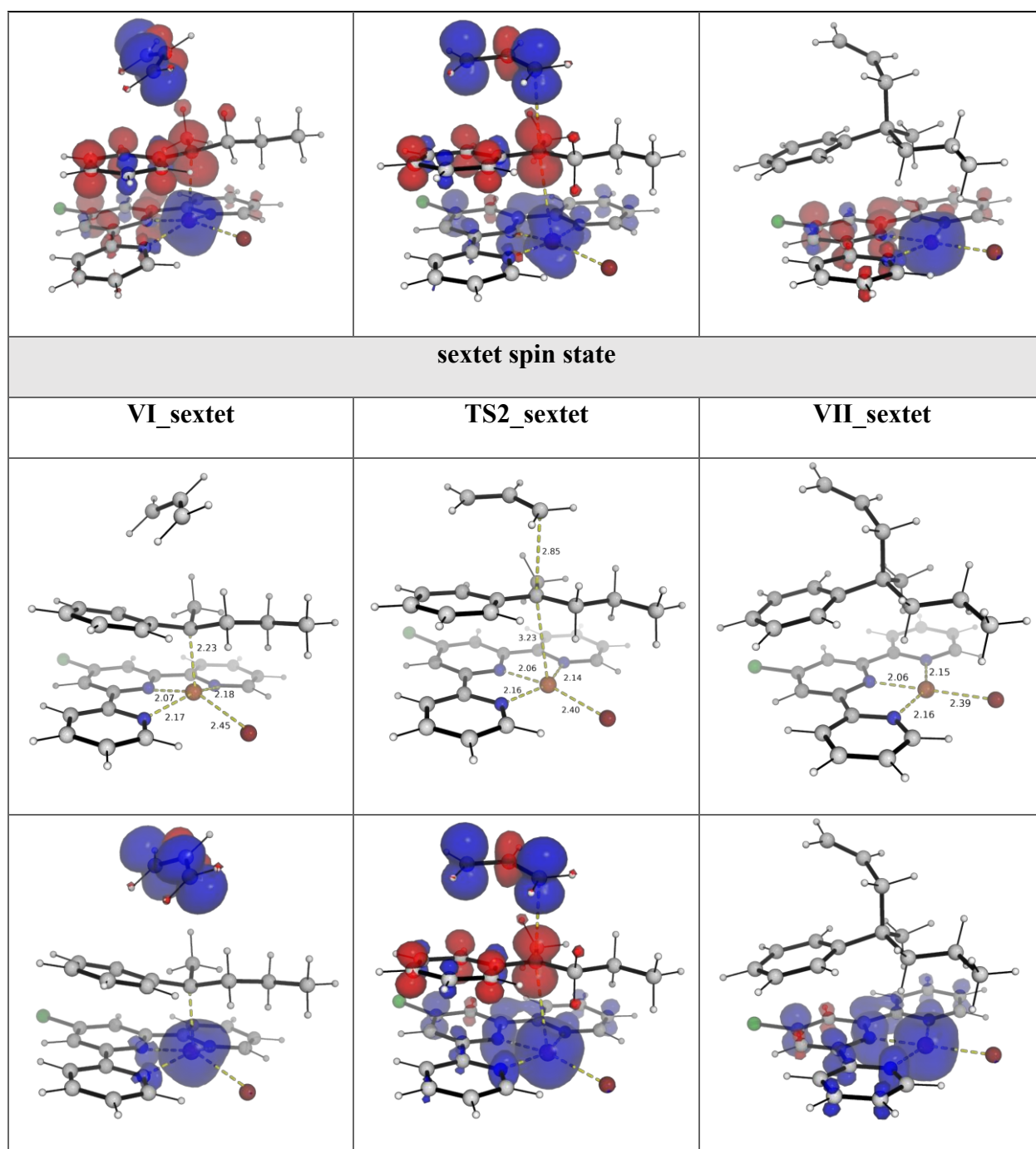


Supplementary Figure 36. Gibbs energy profile for the C–C coupling step via outer-sphere mechanism and the catalyst regeneration steps in different spin states. The superscript on the left indicates the spin states, 1 = singlet; 2 = doublet; 3 = triplet; 4 = quartet; 5 = quintet; 6 = sextet. L = ligand as shown in Supplementary Figure 19.

The DFT optimised structures and the spin density showing the localisation of radical is shown in Supplementary Figure 37. In the reactant state for all spin states, the radical is predominantly located on the allyl fragment and Fe(II) centre whereas in the product state for all spin states, the radical is only localised on the resultant [LFe(I)Br] species, with no radical on the C–C coupled product, which is in close shell, as expected.

Interestingly, the Fe–C and C–C bond lengths are rather elongated in the TSs for all spin states.





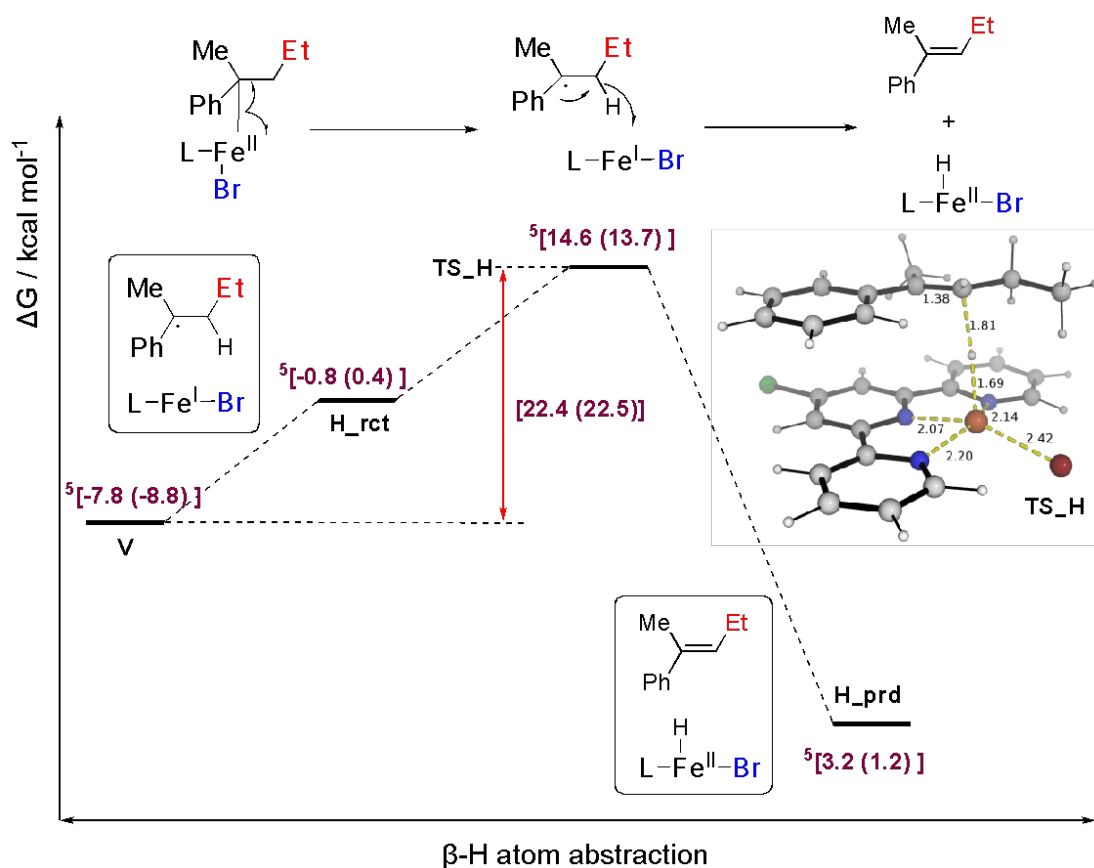
Supplementary Figure 37. DFT-optimized structures for C–C coupling step via outer-sphere mechanism in all spin state and their spin density plots (at an isovalue of 0.02 a.u.).

7.3.8 Side product formation via β -H atom abstraction

We performed DFT studies to understand the formation of the alkene side product observed under the standard reaction conditions. The Gibbs energy profile is shown in Supplementary Figure 38. We found that a feasible mechanism occurs when complex **V** undergoes Fe–C homolysis to give complex **H_{ret}**. This complex then undergoes β -

H atom abstraction via **TS_H** to give the observed olefin side product complexed to the iron hydride species [LFe(II)HBr]. **TS_H** has a barrier of 22.4 (22.5) kcal/mol while the competing mechanism for the formation of the major product via **TS2** in Supplementary Figure 36 has a barrier of 21.8 (20.3) kcal/mol. We note that (THF)-B3LYP-D3BJ/def2-TZVP//B3LYP-D3BJ/def2-SVP Gibbs energies predicts that the formation of major product will be more kinetically favourable than the formation of minor product by 0.6 kcal/mol whereas SMD (THF)-MN15/def2-TZVP//B3LYP-D3BJ/def2-SVP would predict a value of 2.2 kcal/mol. Assuming simple transition state theory, the experimentally observed product ratio of ~8:1 would translate to a barrier difference of about 1.4 kcal/mol, in favour of the major product. We note that this small barrier difference may be difficult to be predicted accurately, as it may fall within the accuracy level possible via DFT and also that simple transition state theory may not work perfectly. Nevertheless, due to the cancellation of errors as we are predicting $\Delta\Delta G^\ddagger$, we conclude that the predicted barrier difference of 0.6 (2.2) kcal/mol agrees reasonably with our experimentally observed product selectivity.

A concerted β -H elimination mechanism could not be found via DFT. However, we hypothesized that this alternative inner-sphere mechanism may be higher in barrier than the one we have located, much in the same way that the concerted inner-sphere migratory insertion (**TS1a**) and reductive elimination (**TS2a**) have higher barriers than their outer-sphere counterparts with radical mechanism (**TS1** and **TS2**, respectively).

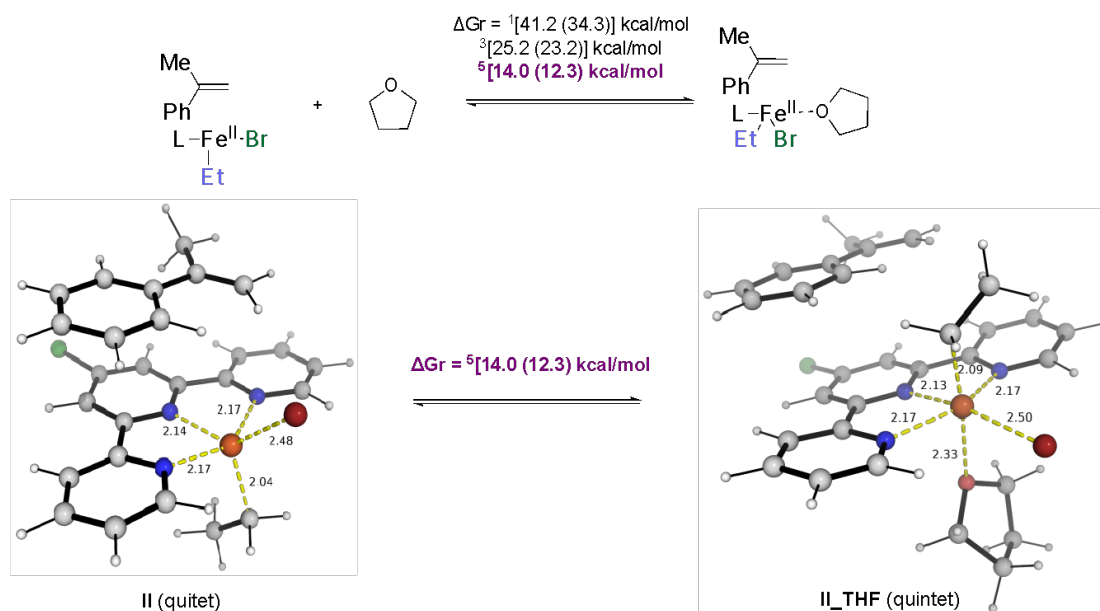


Supplementary Figure 38. Gibbs energy profile for the β -H atom abstraction to give the minor product. DFT optimized structure is shown. The superscript on the left indicates the spin states, 5 = quintet. L = ligand as shown in Supplementary Figure 19.

7.3.9 Consideration of explicit THF solvent molecule participation in the reaction in light of Mössbauer studies

Our freeze-trapped solution-state Mössbauer spectrum of the catalytic reaction after 1 h, 6 h and 12 h indicated the presence of 22% (Supplementary Figure 16), 10% (Supplementary Figure 17) and 8% (Supplementary Figure 18) of $\text{LFe(II)Br}_2\text{THF}$, where solvent molecule THF is coordinated to the reactive species LFe(II)Br_2 . We note that even towards the end of reaction at 12 h, we were still able to residual 8% of this complex, indicating that this species may be stable and may not participate directly in the reaction (it may participate in the reaction by first dissociating the coordinated THF molecule before further reaction). To discern if solvent may directly participate in the reaction, we consider complex **II** in the presence of one molecule of THF coordination. We performed DFT optimisation for all spin states (singlet, triplet and quintet) and found that the formation of the coordination complex **II_THF** in all spin states are

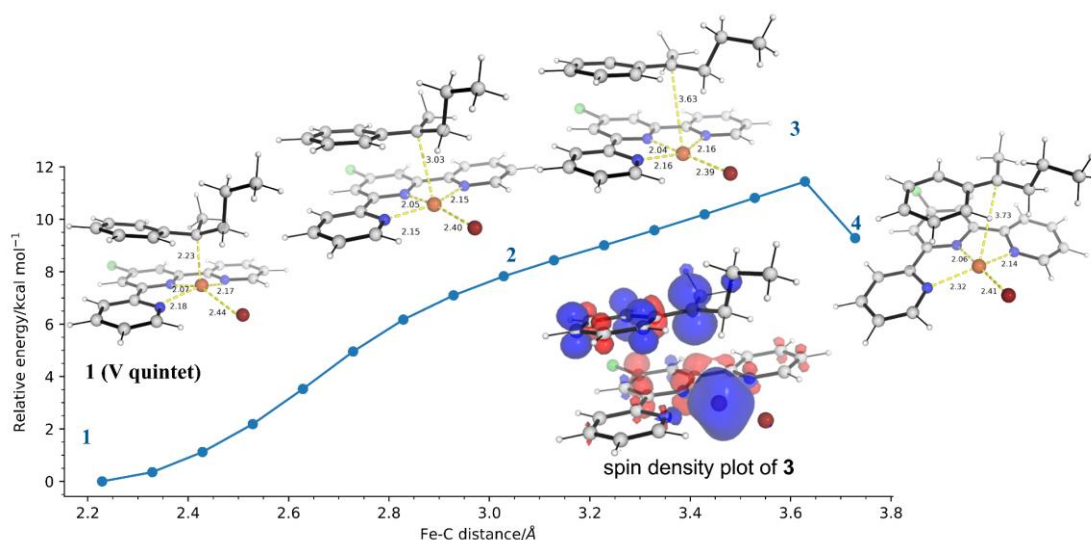
thermodynamically uphill (Figure S39), with the quintet state being least thermodynamically unfavourable (uphill by 14.0 (12.3) kcal/mol). This suggests that the catalytic reaction cycle may not involve explicit solvent participation. In addition, we note that the coordination of THF solvent would take away one coordination site, rendering inner-sphere reaction impossible.



Supplementary Figure 39. Gibbs energy of reaction for the coordination of THF molecule to complex II. DFT optimized structures are shown. The superscript on the left indicates the spin states, 1= single; 3 = triplet; 5 = quintet. L = ligand as shown in Supplementary Figure 19.

7.3.10 Homolytic cleavage of Fe–C bond in intermediate V

We performed a relaxed PES scan along the Fe–C bond in intermediate V (Supplementary Figure 40) and found that it can reversibly break homolytically giving a radical character on the tertiary alkyl carbon. This is estimated to have an energy barrier of 11 kcal/mol. The spin density of the species (structure 3) is also shown. In structure 4, the alkyl group is dissociated and displaced from the Fe center.



Supplementary Figure 40. Relaxed PES scan (in gas-phase using B3LYP-D3BJ/def2-SVP) energy profile along the Fe–C(alkyl) bond in V in quintet state.

Iron(I) pathway

7.4.1 Migratory Insertion step

7.4.1.1 Concerted mechanism

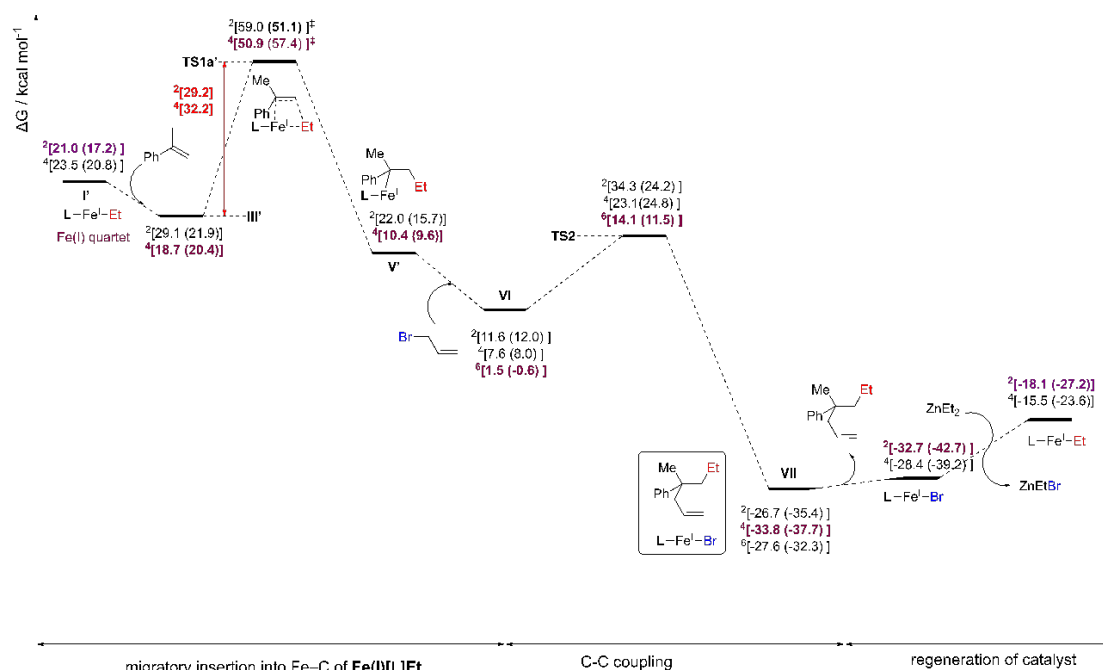
Common reference point for both Fe(II) and Fe(I) pathways

The reductive elimination step resulting from Fe(III) species in complex **VI**/**VI'** in the Fe(I) pathway will be the same as that discussed earlier for the Fe(II) pathway (section 7.3.3). We first take the reference of the Gibbs energy profile for the migratory insertion step involving Fe(I) species the same as that in Fe(II) pathway, in that we keep the energy of complex **VI**/**VI'** to be the same. This energy profile is given in Supplementary Figure 41.

The Fe(I) species **Fe(I)[L]Et (I')** is the most stable in the quartet spin state (**I'**_doublet) and is lower in energy by 2.5 (3.6) kcal/mol compared to its doublet spin state (**I'**_quartet). The migratory insertion step of styrene in the quartet spin state, **TS1a'**_quartet, has a barrier that is 8.1 kcal/mol lower than the migratory insertion step in the doublet state, **TS1a'**_doublet ($\Delta\Delta G^\ddagger = 8.1$ kcal/mol; by Curtin-Hammett principle, the most stable reactant complex is the quartet state **III'**_quartet) using (THF)-B3LYP-D3BJ/def2-TZVP//B3LYP-D3BJ/def2-SVP level of theory whereas **TS1a'**_doublet has a barrier that is 6.3 kcal/mol than **TS1a'**_quartet, using SMD (THF)-MN15/def2-TZVP//B3LYP-D3BJ/def2-SVP level of theory. Nevertheless, both

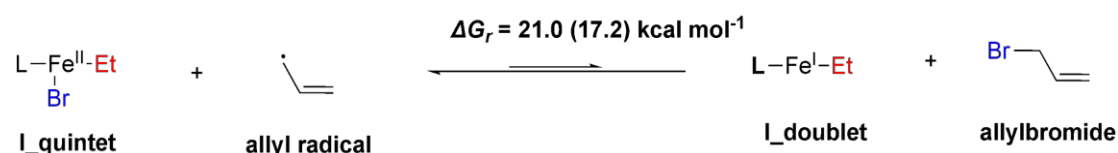
functionals predict similar barrier for Fe(I) pathway: doublet barrier of 29.2 kcal/mol and quartet barrier of 32.2 kcal/mol.

As the generation of catalyst **I'**, **Fe(I)[L]Et** in the quartet state is thermodynamically uphill from **Fe(II)[L]Br**, the overall energetic span for this Fe(I) pathway is 43.8 (44.7) kcal/mol. This is because for this pathway, the turnover-frequency (TOF) determining intermediate (TDI) is **VII** and the TOF-determining transition state (TDTS) is **TS1a'** and that TDI occurs after TDTS (35).



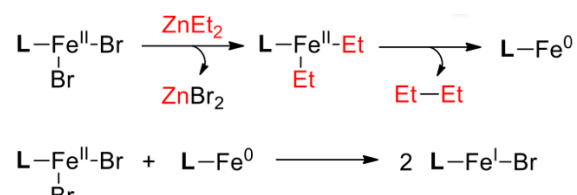
Supplementary Figure 41. Gibbs energy profile for the migratory insertion step of styrene substrate into Fe(I) species in different spin states and the subsequent reductive elimination at Fe(III) center, with the regeneration of the catalyst step. The superscript on the left indicates the spin states, 2 = doublet; 4 = quartet; 6 = sextet. L = ligand as shown in Supplementary Figure 19. Same zero energy reference point is used as in Supplementary Figure 20.

Having the same reference for both the Fe(II) and Fe(I) pathways implies that there is possible interconversion of species **I**, **Fe(II)[L]EtBr** and species **I'**, **Fe(I)[L]Et**. The Gibbs energy of reaction for the following was found to be 21.0 (17.2) kcal/mol uphill for the following conversion:

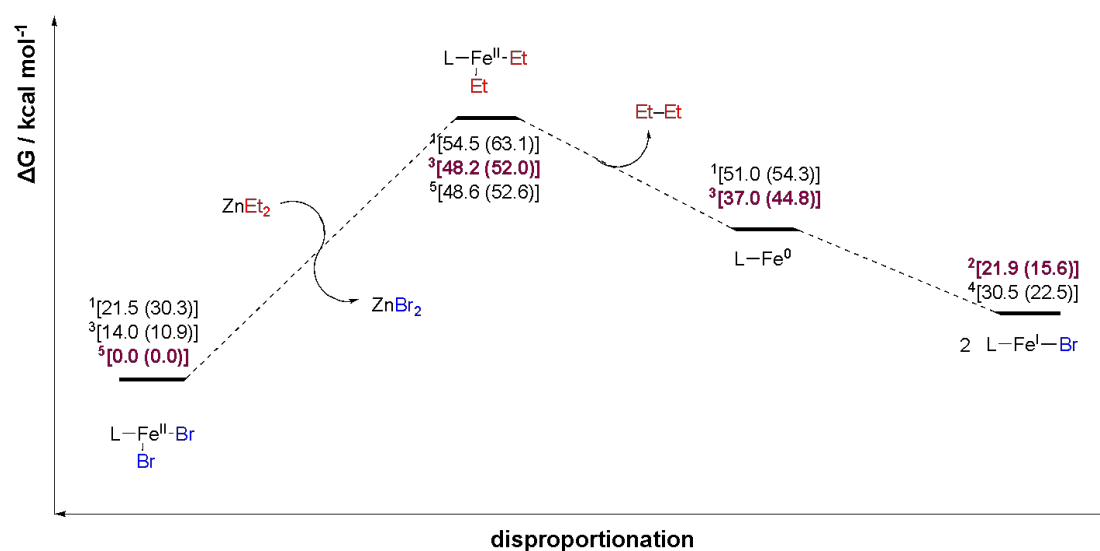


7.4.1.2 Generation of Fe(I) species from disproportionation reaction

We consider if species **I'**, **Fe(I)[L]Et** can be generated favourably by considering the following transformation:



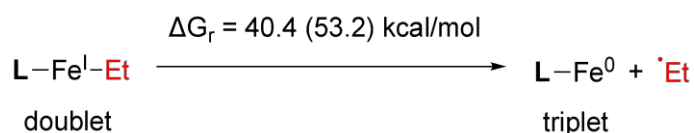
Supplementary Figure 42 shows the energy profile for these transformations. This suggests that this pathway for the formation of Fe(I) species from Fe(II) starting material via disproportionation is both kinetically and thermodynamically unfavourable.



Supplementary Figure 42. Gibbs energy profile for the formation of Fe(I) species from the disproportionation reaction between Fe(II) and Fe(0) species. The superscript on the left indicates the spin states, 1 = singlet; 2 = doublet; 3 = triplet; 4 = quartet; 5 = quintet. **L** = ligand as shown in Supplementary Figure 19. Different zero energy reference point is used as in Supplementary Figure 20.

7.4.1.3 Stepwise mechanism

The generation of ethyl radical from Fe(I) species **I'** has very unfavourable thermodynamics that is uphill by 40.4 (53.2) kcal/mol:



Thus, reaction proceeding via this mechanism is ruled out by DFT.

Optimised structures and absolute energies, zero-point energies

Geometries of all optimized structures (in .xyz format with their associated gas-phase energy in Hartrees) are included in a separate supplementary folder named *final_DFT_structures*. All these data have also been uploaded to <https://zenodo.org/record/8174459>).

Absolute values (in Hartrees) for SCF energy, zero-point vibrational energy (ZPE), enthalpy and quasi-harmonic Gibbs free energy (at 60°C/333.15 K) for optimized structures are given below. Single point corrections in SMD THF using B3LYP-D3BJ/def2-TZVP and MN15/def2-TZVP levels of theory are also included.

Structure	E/au	ZPE/au	H/au	T.S/au	qh-G/au	SP SMD(THF) -B3LYP- D3BJ/def2- TZVP	SP SMD(THF)- MN15/def2- TZVP
allyl_radical	-117.184388	0.065794	-117.11296	0.03086	-117.143821	-117.319582	-117.1411401
allylbromide	-2691.102186	0.070596	-2691.0247	0.036823	-2691.061324	-2691.557039	-2691.682517
bromine_atom	-2573.826536	0	-2573.8239	0.018246	-2573.842144	-2574.144854	-2574.447905
butane	-158.357379	0.131325	-158.2181	0.036535	-158.25457	-158.537672	-158.288206
ethyl_radical	-79.10549	0.058824	-79.040996	0.02978	-79.070687	-79.197808	-79.0697328
Fe0_L_single t	-2465.049587	0.218276	-2464.8115	0.066215	-2464.876143	-2466.219281	-2465.207873
Fe0_L_triplet	-2465.090939	0.216369	-2464.8541	0.06924	-2464.921427	-2466.237621	-2465.219068
Fe1_L_Br_doublet	-5039.076075	0.219821	-5038.8338	0.07442	-5038.905543	-5040.539671	-5039.841705
Fe1_L_Br_quartet	-5039.067702	0.218198	-5038.8264	0.078117	-5038.900606	-5040.529396	-5039.832748
Fe1_L_Et_doublet	-2544.289559	0.281756	-2543.9829	0.078848	-2544.058339	-2545.526791	-2544.400548
Fe1_L_Et_quartet	-2544.277239	0.281318	-2543.9711	0.079408	-2544.047125	-2545.52163	-2544.393723
Fe2_L_Et_Et _quintet	-2623.448833	0.344362	-2623.0741	0.093162	-2623.162051	-2624.771258	-2623.509355

Fe2_L_Et_Et_singlet	-2623.443572	0.348478	-2623.066	0.088812	-2623.149411	-2624.769189	-2623.499995
Fe2_L_Et_Et_triplet	-2623.455133	0.346479	-2623.0793	0.088137	-2623.16372	-2624.77647	-2623.514924
FeBr2_L_quintet	-7613.021224	0.221361	-7612.7744	0.085951	-7612.854697	-7614.812639	-7614.412735
FeBr2_L_singlet	-7612.988275	0.223224	-7612.7407	0.082168	-7612.817296	-7614.782875	-7614.368922
FeBr2_L_triplet	-7612.995852	0.223304	-7612.7479	0.082715	-7612.825658	-7614.794069	-7614.399035
H_prd	-5467.010764	0.444922	-5466.5267	0.114474	-5466.63238	-5468.948566	-5467.627313
H_rct	-5467.034	0.448867	-5466.5465	0.112267	-5466.651281	-5468.959292	-5467.632963
I_quintet	-5118.236005	0.282983	-5117.9251	0.089217	-5118.009069	-5119.793086	-5118.964705
I_quintet_c2	-5118.237364	0.28331	-5117.9263	0.088148	-5118.009681	-5119.787534	-5118.960331
I_singlet	-5118.230121	0.287133	-5117.9168	0.082027	-5117.994945	-5119.78458	-5118.948512
I_singlet_c2	-5118.229068	0.28691	-5117.916	0.081804	-5117.993929	-5119.783503	-5118.945898
I_triplet	-5118.229687	0.284767	-5117.9182	0.083929	-5117.998411	-5119.782029	-5118.95233
I_triplet_c2	-5118.227474	0.284596	-5117.916	0.084442	-5117.996598	-5119.779214	-5118.94916
II	-5467.018116	0.446139	-5466.5322	0.116453	-5466.639254	-5468.952811	-5467.626807
II_THF_quintet	-5699.330239	0.564156	-5698.7188	0.132909	-5698.840353	-5701.517916	-5699.892742
II_THF_singlet	-5699.291048	0.569565	-5698.6767	0.12372	-5698.790951	-5701.484674	-5699.867768
II_THF_triplet	-5699.3202	0.565423	-5698.7078	0.132233	-5698.828279	-5701.501985	-5699.877374
IIa_quintet	-5467.011308	0.446142	-5466.5255	0.115687	-5466.632103	-5468.94485	-5467.61986
IIa_singlet	-5466.979242	0.451716	-5466.4909	0.101872	-5466.587723	-5468.913688	-5467.59914
IIa_triplet	-5467.003536	0.447017	-5466.5184	0.110399	-5466.621153	-5468.927398	-5467.605337
IIb	-427.861318	0.221634	-427.62204	0.064571	-427.682394	-428.339003	-427.716325
III_doublet	-5387.860858	0.383269	-5387.4439	0.09824	-5387.536838	-5389.703525	-5388.509299
III_doublet_c2	-5387.859086	0.383226	-5387.4419	0.099097	-5387.535539	-5389.69907	-5388.505898
III_prime_doublet	-2893.068391	0.445928	-2892.5869	0.100833	-2892.682344	-2894.677848	-2893.060992
III_prime_quartet	-2893.077145	0.443651	-2892.5965	0.106749	-2892.696405	-2894.689154	-2893.058131
III_quartet	-5387.870879	0.381777	-5387.4546	0.101888	-5387.550346	-5389.713428	-5388.513147
III_quartet_c2	-5387.851488	0.382025	-5387.4352	0.100966	-5387.530307	-5389.688937	-5388.496711
IIIa_quintet	-5467.042222	0.451396	-5466.5531	0.108051	-5466.655068	-5468.963364	-5467.644659

IIIa_singlet	-5467.017294	0.453407	-5466.5273	0.102921	-5466.624573	-5468.947506	-5467.626728
IIIa_triplet	-5467.02938	0.452652	-5466.5398	0.10463	-5466.639191	-5468.952714	-5467.627079
IIIb	-427.916047	0.227908	-427.67312	0.056144	-427.727567	-428.389968	-427.76889
INT2_Br_quintet	-5467.042222	0.451396	-5466.5531	0.108051	-5466.655068	-5468.963364	
IV_quintet	-5466.986462	0.441954	-5466.5033	0.118851	-5466.613168	-5468.916979	-5467.589949
ligand_L	-1201.464448	0.217048	-1201.2285	0.066556	-1201.29191	-1202.453641	-1201.368816
product	-545.194815	0.302734	-544.87296	0.064669	-544.934868	-545.797219	-545.008271
styrene	-348.74936	0.161453	-348.577	0.045305	-348.621543	-349.136984	-348.640964
TS_H	-5467.002441	0.444397	-5466.5203	0.107765	-5466.622177	-5468.932393	-5467.609327
TS1_quintet	-5466.97969	0.44328	-5466.4969	0.114843	-5466.603246	-5468.911253	-5467.580413
TS1_singlet_openshell	-5466.960888	0.445414	-5466.477	0.109384	-5466.579061	-5468.893719	-5467.556852
TS1_triplet	-5466.969418	0.444702	-5466.486	0.111484	-5466.589778	-5468.90096	-5467.577305
TS1a_prime_doublet	-2893.025989	0.448067	-2892.5441	0.095296	-2892.635479	-2894.634655	-2893.018858
TS1a_prime_quartet	-2893.030018	0.444375	-2892.55	0.102102	-2892.646876	-2894.640112	-2893.00156
TS1a_quintet	-5466.968813	0.447328	-5466.4835	0.108905	-5466.585907	-5468.903165	-5467.578098
TS1a_quintet_g	-5466.95277	0.44591	-5466.4678	0.113515	-5466.573425	-5468.888119	-5467.563775
TS1a_singlet	-5466.961812	0.451446	-5466.4742	0.101518	-5466.570434	-5468.896195	-5467.579893
TS1a_singlet_g	-5466.938641	0.451346	-5466.4508	0.102496	-5466.548058	-5468.871429	-5467.553601
TS1a_triplet	-5466.949879	0.449733	-5466.4633	0.104568	-5466.562341	-5468.887218	-5467.565935
TS1a_triplet_g	-5466.952924	0.449698	-5466.4656	0.108698	-5466.567461	-5468.884877	-5467.564709
TS1b	-427.856275	0.222624	-427.61772	0.059788	-427.674611	-428.334304	-427.708269
TS2_doublet	-5584.222454	0.517159	-5583.6615	0.122786	-5583.774922	-5586.24727	-5584.760445
TS2_quartet	-5584.217125	0.517556	-5583.6561	0.12143	-5583.769206	-5586.265416	-5584.759965
TS2_sextet	-5584.225336	0.516443	-5583.6648	0.124089	-5583.779874	-5586.277395	-5584.77862
TS2a_quartet	-5584.21983	0.515907	-5583.6595	0.126202	-5583.775304	-5586.240268	-5584.780437
TS2a_sextet	-5584.206329	0.51871	-5583.6445	0.121121	-5583.757239	-5586.267733	-5584.766487
V_prime_doublet	-2893.081658	0.448649	-2892.598	0.100231	-2892.692687	-2894.692121	-2893.073723
V_prime_quartet	-2893.093406	0.44755	-2892.6102	0.103071	-2892.707302	-2894.707662	-2893.080622
V_quintet	-5467.049118	0.451005	-5466.5603	0.109021	-5466.662694	-5468.97422	-5467.651292
VI_doublet	-5584.230541	0.519341	-5583.6673	0.123413	-5583.781093	-5586.285242	-5584.781869

VI_quartet	-5584.229431	0.515865	-5583.6681	0.128887	-5583.786096	-5586.285538	-5584.782095
VI_sextet	-5584.242562	0.518113	-5583.6798	0.127065	-5583.79654	-5586.297962	-5584.798401
VIa_doublet	-5584.234004	0.524238	-5583.6677	0.114772	-5583.776126	-5586.295645	-5584.803821
VIa_quartet	-5584.250463	0.522026	-5583.6852	0.120088	-5583.797658	-5586.312725	-5584.81812
VII_doublet	-5584.295044	0.524888	-5583.7276	0.121436	-5583.839086	-5586.352861	-5584.86384
VII_quartet	-5584.304195	0.522841	-5583.7379	0.12457	-5583.852013	-5586.360362	-5584.863778
VII_sextet	-5584.298942	0.522384	-5583.7331	0.124857	-5583.847641	-5586.349618	-5584.854339
VIIa_quartet	-5584.303615	0.52275	-5583.7376	0.124708	-5583.851477	-5586.359986	-5584.837141
VIIa_sextet	-5584.297963	0.522422	-5583.7321	0.125179	-5583.846626	-5586.354174	-5584.858513
Viprime_a_doublet	-5584.241472	0.519563	-5583.6779	0.123776	-5583.791751	-5586.306617	-5584.801331
Viprime_a_quartet	-5584.242594	0.519749	-5583.6789	0.124086	-5583.793154	-5586.306809	-5584.79993
Viprime_a_sextet	-5584.242018	0.517945	-5583.6789	0.130097	-5583.797341	-5586.312331	-5584.81229
ZnBr2	-6927.049095	0.001734	-6927.0416	0.034178	-6927.075203	-6927.947907	-6928.793892
ZnEt2	-1937.523281	0.127817	-1937.3844	0.048827	-1937.430573	-1937.982556	-1937.972871
ZnEtBr	-4432.292191	0.065131	-4432.2185	0.041901	-4432.259673	-4432.972685	-4433.38986

Supplementary References

1. Liang, Q.-J. *et al.* Chelation versus non-chelation control in the stereoselective alkenyl sp² C–H bond functionalization reaction. *Angew. Chem. Int. Ed.* **56**, 5091–5095 (2017).
2. Zhao, Z., Racicot, L. & Murphy, G. K. Fluorinative rearrangements of substituted phenylallenes mediated by (difluoroiodo) toluene: synthesis of α -(difluoromethyl) styrenes. *Angew. Chem. Int. Ed.* **56**, 11620–11623 (2017).
3. Jiang, Y.-M. *et al.* Electrochemical fluorosulfonylation of styrenes. *Chem. Commun.* **57**, 11481–11484 (2021).
4. Xiong, P. *et al.* Electrochemically enabled carbohydroxylation of alkenes with H₂O and organotrifluoroborates. *J. Am. Chem. Soc.* **140**, 16387–16391 (2018).
5. Liu, C.-F. *et al.* Synthesis of tri- and tetrasubstituted stereocentres by nickel-catalysed enantioselective olefin cross-couplings. *Nat. Catal.* **5**, 934–942 (2022).
6. Wang, D., Xue, X.-S., Houk, K. N. & Shi, Z. Mild ring-opening 1, 3-hydroborations of non-activated cyclopropanes. *Angew. Chem. Int. Ed.*, **57**, 16861–16865 (2018).
7. Phan, D. H., Kou, K. G. & Dong, V. M. Enantioselective desymmetrization of cyclopropenes by hydroacylation. *J. Am. Chem. Soc.* **132**, 16354–16355 (2010).
8. Barluenga, J., Trincado, M., Rubio, E. & González, J. M. Intramolecular arylation reactions of alkenes: A flexible approach to chromans and tetrahydroquinoline derivatives. *J. Am. Chem. Soc.* **126**, 3416–3417 (2004).
9. Takaya, J., Sasano, K. & Iwasawa, N. Efficient one-to-one coupling of easily available 1, 3-dienes with carbon dioxide. *Org. Lett.* **13**, 1698–1701 (2011).
10. Bertrand, X. & Paquin, J.-F. Direct hydrofluorination of methallyl alkenes using a methanesulfonic acid/triethylamine trihydrofluoride combination. *Org. Lett.* **21**, 9759–9762 (2019).
11. Lin, Y. A., Chalker, J. M., Floyd, N., Bernardes, G. J. & Davis, B. G. Allyl sulfides are privileged substrates in aqueous cross-metathesis: application to site-selective protein modification. *J. Am. Chem. Soc.* **130**, 9642–9643 (2008).
12. Wang, Y., Yang, Y. & Wang, C. Rhenium-catalyzed decarboxylative tri-/difluoromethylation of styrenes with fluorinated carboxylic acid-derived hypervalent iodine reagents. *Chin. J. Chem.* **37**, 1229–1233 (2019).

13. Fuchibe, K. *et al.* Domino Friedel–Crafts-type cyclizations of difluoroalkenes promoted by the α -cation-stabilizing effect of fluorine: an efficient method for synthesizing angular PAHs. *Chem. Eur. J.* **17**, 12175–12185 (2011).
14. Mazuela, J. *et al.* Iridium phosphite-oxazoline catalysts for the highly enantioselective hydrogenation of terminal alkenes. *J. Am. Chem. Soc.* **131**, 12344–12353 (2009).
15. Liu, H., Ge, L., Wang, D.-X., Chen, N. & Feng, C. Photoredox-coupled F-nucleophilic addition: allylation of gem-difluoroalkenes. *Angew. Chem. Int. Ed.* **58**, 3918–3922 (2019).
16. Yang, B. & Lu, Z. Visible light-promoted dihydroxylation of styrenes with water and dioxygen. *Chem. Commun.* **53**, 12634–12637 (2017).
17. Neufeld, J., Stnkel, T., Mck-Lichtenfeld, C., Daniliuc, C. G. & Gilmour, R. Trifluorinated tetralins via I(I)/I(III)-catalysed ring expansion: programming conformation by $[\text{CH}_2\text{CH}_2] \rightarrow [\text{CF}_2\text{CHF}]$ isosterism. *Angew. Chem. Int. Ed.* **60**, 13647–13651 (2021).
18. Liu, K. & Studer, A. Direct α -acylation of alkenes via N-heterocyclic carbene, sulfinate, and photoredox cooperative triple catalysis. *J. Am. Chem. Soc.* **143**, 4903–4909 (2021).
19. Huang, Z., Wang, Y., Leng, X. & Huang, Z. An amine-assisted ionic monohydride mechanism enables selective alkyne cis-semihydrogenation with ethanol: from elementary steps to catalysis. *J. Am. Chem. Soc.* **143**, 4824–4836 (2021).
20. Kleinbeck, F. & Toste, F. D. Gold (I)-catalyzed enantioselective ring expansion of allenylcyclopropanols. *J. Am. Chem. Soc.* **131**, 9178–9179 (2009).
21. Meyer, M. P. & Klinman, J. P. Investigating inner-sphere reorganization via secondary kinetic isotope effects in the C–H cleavage reaction catalyzed by soybean lipoxygenase: tunneling in the substrate backbone as well as the transferred hydrogen. *J. Am. Chem. Soc.* **133**, 430–439 (2011).
22. Dinca, E. *et al.* General and efficient α -oxygenation of carbonyl compounds by TEMPO induced by single-electron-transfer oxidation of their enolates. *Eur. J. Org. Chem.* 4461–4482 (2012).
23. Krasovskiy, A. & Knochel, P. Convenient titration method for organometallic zinc, magnesium, and lanthanide reagents. *Synthesis* **5**, 890–891 (2006).

24. Beves, J. E. *et al.* 4'-Chloro-2,2':6',2"-terpyridine (L): ethyl sulfate salts of $[H_2L]^{2+}$ and the single crystal structures of $[H_2L][EtOSO_3]Cl \cdot H_2O$ and $[ML_2][PF_6]_2$ with $M = Fe$ and Ru . *Inorg. Chem. Commun.* **11**, 1006–1008 (2008).
25. Reiff, W. M., Erickson, N. E. & Baker Jr., W. A. Mono(2,2',2"-terpyridine) complexes of iron(II). *Inorg. Chem.* **8**, 2019–2021 (1969).
26. Waibel, M. *et al.* Bibenzyl- and stilbene-core compounds with non-polar linker atom substituents as selective ligands for estrogen receptor beta. *Eur. J. Med. Chem.* **44**, 3412–3424 (2009).
27. Sakaguchi, H. *et al.* Copper-catalyzed regioselective monodefluoroborylation of polyfluoroalkenes enroute to diverse fluoroalkenes. *J. Am. Chem. Soc.* **139**, 12855–12862 (2017).
28. Gasparyan, N. K., Gevorgyan, G. A., Paronikyan, R. G., Tumadzhyan, A. E. & Panosyan, G. A. Synthesis and biological activity of diaryl-substituted 3-morpholinopropanols. *Pharm. Chem. J.* **39**, 361–363 (2005).
29. Zhang, W. *et al.* Electrochemically driven cross-electrophile coupling of alkyl halides. *Nature* **604**, 292–297 (2022).
30. Li, P., Zbieg, J. R., Terrett, J. A. A Platform for decarboxylative couplings via photoredox catalysis: direct access to carbocations from carboxylic acids for carbon–oxygen bond formation. *ACS Catal.* **11**, 10997–11004 (2021).
31. Brennan-Wydra, S. F. E., MacLeod, K. C. & Holland, P. L. Density functional calculations for prediction of ^{57}Fe Mössbauer isomer shifts and quadrupole splittings in β -diketiminato complexes. *ACS Omega* **2**, 2594–2606 (2017).
32. Frisch, M. J. *et al.* *Gaussian, Inc., Wallingford CT, Gaussian 16, Revision B.01.* (2016).
33. Becke, A. D. Density-functional thermochemistry. III. The role of exact exchange. *J. Chem. Phys.* **98**, 5648–5652 (1993).
34. Lee, C., Yang, W. & Parr, R. G. Development of the colle-salvetti correlation-energy formula into a functional of the electron density. *Phys. Rev. B* **37**, 785–789 (1988).
35. Vosko, S. H., Wilk, L. & Nusair, M. Accurate spin-dependent electron liquid correlation energies for local spin density calculations: a critical analysis. *Can. J. Phys.* **58**, 1200–1211 (1980).

36. Stephens, P. J., Devlin, F. J., Chabalowski, C. F. & Frisch, M. J. Ab initio calculation of vibrational absorption and circular dichroism spectra using density functional force fields. *J. Phys. Chem.* **98**, 11623–11627 (1994).
37. Grimme, S., Antony, J., Ehrlich, S. & Krieg, H. A consistent and accurate Ab initio parametrization of density functional dispersion correction (DFT-D) for the 94 elements H-Pu. *J. Chem. Phys.* **132**, 154104 (2010).
38. Weigend, F. & Ahlrichs, R. Balanced basis sets of split valence, triple zeta valence and quadruple zeta valence quality for H to Rn: design and assessment of accuracy. *Phys. Chem. Chem. Phys.* **7**, 3297–3305 (2005).
39. Fukui, K. The path of chemical reactions - the IRC approach. *Acc. Chem. Res.* **14**, 363–368 (1981).
40. Fukui, K. Formulation of the reaction coordinate. *J. Phys. Chem.* **74**, 4161–4163 (2005).
41. Marenich, A. V., Cramer, C. J. & Truhlar, D. G. Universal solvation model based on solute electron density and on a continuum model of the solvent defined by the bulk dielectric constant and atomic surface tensions. *J. Phys. Chem. B* **113**, 6378–6396 (2009).
42. Grimme, S. Supramolecular binding thermodynamics by dispersion-corrected density functional theory. *Chem. Eur. J.* **18**, 9955–9964 (2012).
43. Luchini, G., Alegre-Requena, J. V., Funes-Ardoiz, I., Paton, R. S. & Pollice, R. GoodVibes: automated thermochemistry for heterogeneous computational chemistry data. *F1000Research* **9**, 291 (2020).
44. Bryantsev, V. S., Diallo, M. S. & Goddard, W. A. Calculation of solvation free energies of charged solutes using mixed cluster/continuum models. *J. Phys. Chem. B* **112**, 9709–9719 (2008).
45. Boyle, B. T., Levy, J. N., de Lescure, L., Paton, R. S. & McNally, A. Halogenation of the 3-position of pyridines through zinc imine intermediates. *Science* **378**, 773–779 (2022).
46. Darù, A., Hu, X. & Harvey, J. N. Iron-catalyzed reductive coupling of alkyl iodides with alkynes to yield cis-olefins: mechanistic insights from computation. *ACS Omega* **5**, 1586–1594 (2020).
47. Yu, H. S., He, X., Li, S. L. & Truhlar, D. G. MN15: A Kohn–Sham global-hybrid exchange–correlation density functional with broad accuracy for multi-reference

- and single-reference systems and noncovalent interactions. *Chem. Sci.* **7**, 5032–5051 (2016).
48. Dandu, N. K., Reed, J. A. & Odoh, S. O. Performance of density functional theory for predicting methane-to-methanol conversion by a tri-copper complex. *J. Phys. Chem. C* **122**, 1024–1036 (2018).
49. Schrödinger, L. *The PyMOL Molecular Graphics Development Component, Version 1.8* (2015).
50. Dennington, R., Keith, T. A. & Millam, J. M. GaussView, Version 6.1, Semichem Inc., Shawnee Mission, KS (2016).